

Nanometer-precision tracking of adipocyte dynamics via single lipid droplet whispering-gallery optical resonances

Rok Podlipec^{1*}, Ana Krišelj¹, Maja Garvas Zorc¹, Petra Matjan Štefin^{2,3}, Siegfried Usaar⁴, Matjaž Humar^{1,5,6}

¹ Department of Condensed Matter Physics, Jozef Stefan Institute, Jamova 39, SI-1000 Ljubljana, Slovenia

² Department of Biochemistry and Molecular and Structural Biology, Jozef Stefan Institute, Jamova cesta 39, SI-1000 Ljubljana, Slovenia

³ Jozef Stefan International Postgraduate School, Jamova cesta 39, SI-1000 Ljubljana, Slovenia

⁴ Research Unit Adipocytes & Metabolism (ADM), Helmholtz Diabetes Center, Helmholtz Zentrum München, Germany; Research Center for Environmental Health GmbH, Neuherberg 85764, Germany

⁵ Faculty of Mathematics and Physics, University of Ljubljana, Jadranska 19, SI-1000 Ljubljana, Slovenia

⁶ CENN Nanocenter, Jamova 39, SI-1000 Ljubljana, Slovenia

Corresponding author: rok.podlipec@ijs.si

Abstract

Biophotonics—and more recently, biointegrated photonics—offer transformative tools for probing cellular processes with unprecedented precision. Among these, whispering gallery mode (WGM) resonators—optical microcavities formed in spherical structures—have emerged as powerful biosensors and intracellular barcodes. Lipid droplets (LDs), with their high refractive index and intrinsic spherical geometry, are ideal candidates for supporting intracellular lasing. Although lasing in LDs has been previously demonstrated, it has not yet been harnessed to study live cell biology. Here, we report the first use of WGM resonances in LDs of live primary adipocytes, employing a continuous-wave (CW) laser at powers below the biological damage threshold. By measuring these resonances, we achieved nanometer-scale precision in size estimation, enabling real-time observation of rapid LD dynamics and deformations on the minute scale—far beyond the spatio-temporal resolution of conventional microscopy. We systematically characterized this photonic sensing approach, demonstrating its ability to resolve adipocyte heterogeneity, monitor lipolytic responses to forskolin and isoproterenol, and detect early signs of cell viability loss—well before conventional assays. This proof-of-concept establishes intracellular LD WGM resonances as a robust platform for investigating live single-cell metabolism. The technique enables rapid, cost-effective

assessment of adipocyte function, reveals cell-to-cell variability obscured by bulk assays, and lays the foundation for high-throughput analysis of metabolism- and obesity-related diseases at both cellular and tissue levels.

Keywords — adipocyte dynamics, lipid droplets, whispering gallery modes, optical resonances, lipolysis

1. Introduction

Biointegrated photonics and biophotonics are rapidly emerging fields in cellular sensing, leveraging advanced optical technologies to study and manipulate biological processes with exceptional precision ¹. One of the highly promising biosensing strategy employs whispering gallery mode (WGM) resonators ^{2,3}, which exploit optical resonances in spherical objects, such as microspheres and microdroplets. Light waves induced and propagated within these cavities undergo continuous internal reflection along the concave surface, producing constructive interference ⁴. The resonant conditions—capable of achieving extremely high quality (Q) factors—depend on the refractive index contrast between the cavity and its surrounding environment and exponentially on the microcavity size ⁵. These unique properties have enabled a broad spectrum of applications in biological and physical sensing ^{4,6–8}, offering remarkable sensitivity for detecting subtle changes at the single-cell ⁹ and single-molecule levels ^{10–12}. Applications range from detecting single proteins and silica nanobead binding ¹⁰, to plasmon-enhanced sensing with nanorods for short nucleic acid strands ¹¹, and even single-virus tracking ¹³. More recently, significant attention has been directed toward intracellular probing techniques for cell tagging, barcoding, and tracking ^{14–19}, cavity-enhanced bioluminescence ²⁰, and investigations into cellular (patho)physiology, including cardiac contractility ²¹ and molecular binding ²².

Despite the promise of this emerging research frontier, intracellular studies utilizing biointegrated microlasers remain limited, particularly in addressing biologically relevant questions such as complex cell heterogeneity in disease contexts ⁹. One highly underexplored yet potentially transformative approach involves lasing on endogenous cellular structures. Lipid droplets (LDs), owing to their high sphericity and elevated refractive index relative to the surrounding cytoplasm, are capable of supporting intracellular lasing ¹⁴. Lasing in LDs is feasible for droplets larger than approximately 25 μm , where radiative losses are sufficiently minimized. This could make adipose tissue (AT)—which contains LDs of the sizes ranging up to 100 μm and more in mature adipocytes ²³—an ideal candidate for such applications. However, to date, intracellular lasing in LDs has not been applied to the study of adipocytes.

LDs primarily serve as reservoirs for lipids—essential components for maintaining metabolic energy reserves and supplying lipids for cellular membranes²⁴. Although central to adipocyte function, the role of LD metabolism and its dysregulation in metabolic diseases remains underexplored²⁵. It is now recognized that LDs play multiple roles in systemic homeostasis and obesity-related pathologies^{26–29}, extending far beyond fat storage. They act as dynamic hubs for lipid management, integrating metabolic signals and lipid fluxes with diverse cellular homeostatic and stress responses³⁰. Despite their critical role in AT regulation, the dynamic nature and biological activity of LDs are still poorly understood³¹. Current data are largely limited to single-cell gene expression analyses³² and bulk functional assays, such as lipolysis kits applied to large populations of adipocytes³³. These approaches fail to capture the heterogeneity of LD function and dynamics both within and between individual cells. Moreover, averaging LD behavior across cell populations obscures the contributions of individual organelles, limiting our understanding of their nuanced/complex roles.

To overcome these limitations novel optical methods are needed to assess LD dynamics in living, single primary adipocytes from animal or human sources. In recent years, several experimental approaches have emerged, including morphology-oriented live-cell and single-cell imaging of LDs using fluorescence microscopy^{34,35}, the development of advanced fluorescent probes³⁶, label-free Raman microscopy^{37,38}, as well as machine learning–based tools and analysis³⁹. Although these techniques have enabled the study of metabolic processes at cellular and subcellular levels previously inaccessible⁴⁰, they remain constrained by the optical resolution limit of ~250 nm (Rayleigh criterion), which prevents detection of morphological changes below this threshold. Limited spatial resolution also restricts temporal resolution, making it difficult to capture rapid, nanometer-scale changes in LD size—processes critical for understanding early metabolic shifts and predicting long-term outcomes of LD activity. LD growth (e.g., induced lipogenesis⁴¹) and shrinkage (e.g., induced lipolysis⁴²) are often slow, occurring over hours, days, or even weeks before substantial size changes become detectable via live-cell microscopy⁴³. Achieving nanometer precision in LD size measurements would enable near-instantaneous detection of growth or shrinkage, offering valuable insights into short-term metabolic dynamics.

To address these challenges, we demonstrate and characterize lasing in natural intracellular LDs for the first time, enabling precise tracking of individual LD size. Building on our previously established WGM-based methodology for embedded lasing in live cells¹⁴, this approach offers exceptionally high spatial (sub-nanometer) and temporal (minute-scale) resolution for investigating LD size and dynamics. In this study, we systematically evaluate the methodological and physical aspects of photonic sensing in live, mature adipocytes, emphasizing both its strengths and limitations. Rather than focusing on detailed biological interpretations, our primary goal is to establish the methodological foundation for future

studies. These findings pave the way for advanced metabolic investigations into the highly heterogeneous and dynamic nature of adipocytes and adipose tissue.

2. Materials and methods

MATERIALS.

Visceral fat (isolated from FVB/N female mice), 1x phosphate buffer saline (PBS, Gibco), Dulbecco's Modified Eagle's Medium (DMEM, Gibco), Collagenase IV (Gibco), Fatty Acid Free Bovine Serum Albumin (BSA FAF, Sigma Aldrich), Fetal Bovine Serum (FBS, Gibco), Pyrromethene 597 (Exciton Luxottica), verapamil (Spirochrome), SYTOX Deep Red (Thermo Fischer Scientific), CellMask Deep Red (Thermo Fischer Scientific), Forskolin (Sigma Aldrich), Triacsin (Cayman).

ANIMALS.

Mice were used in accordance with the Administration of the Republic of Slovenia for food safety, veterinary and plant protection (permit number: U34401-5/2022/15). Procedures for animal care and experiments were in accordance with the "Guide for the Care and Use in Laboratory Animals".

METHODS.

Adipocyte isolation. Visceral AT was isolated from FVB/N female mice. After the removal of larger veins, AT was cut into smaller pieces (1-2 mm³) and washed three times in cold PBS. Pieces were transferred in a 25 mL centrifuge tube with DMEM, complemented with penicillin (100 IU/mL), streptomycin (100 µg/mL), 1 mg/mL Collagenase Type IV, and 1% (w/v) BSA (FAF). 2 mL of the collagenase solution was used per 1 g of fat tissue. Minced fat tissue was then incubated at 37 °C for 30-40 min and gently shaken every 10 min to allow for adequate disaggregation and isolation of individual adipocytes, preserving their viability. After digestion was complete, the suspension was mixed on a vortex mixer for 10 seconds to release the remaining cells from the tissue and then passed through a sieve with 100 µm pores. Collagenase was neutralized with the same volume of FBS. The cell suspension was then allowed to separate into layers at 37 °C for 15 minutes due to density differences. The top lipid layer and the bottom medium layer were discarded, followed by carefully pipetting of mature adipocytes into a fresh centrifuge tube, where they were washed 3 times with cell culture medium (DMEM, complemented with penicillin (100 IU/mL), streptomycin (100 µg/mL), 4mM L-Glutamine, 10 % FBS, 0.5 µg/mL insulin, 0.4 ng/mL dexamethasone). Mature adipocytes were cultured in 12-well plates at 37 °C and 5% CO₂. Each well in a 12-well plate was filled with 1 mL of cell culture medium and 200 µL of dense suspension of isolated adipocytes. Medium without insulin and dexamethasone was used for further experiments.

Adipocyte labeling for optical sensing and dynamics studies. The cell suspension was mixed with 1.5 $\mu\text{g/ml}$ (4 μM) pyrromethene 597 BODIPY laser dye for labeling of LDs to enable lasing applications. After a few hours of incubation at 37°C and 5% CO_2 , the cell media containing LDs label was exchanged with the cell media containing CellMask Deep Red (2.5 $\mu\text{g/ml}$, 2000x diluted stock solution) and SYTOX Red (5 nM, 1000x diluted stock solution) for 15 minutes incubated on 37°C and 5% CO_2 . The volume of 1 ml suspension was then exchanged four times with insulin-free cell media to remove non-labeled stains. For the optimal experimental conditions, ceiling translucent trans-well inserts (3 μm pores, Falcon) were carefully immersed and fixated inside the 12-wells, where a significant part of the densely populated floating adipocytes remained confined beneath the porous surface (Figure 1). For studying adipocyte dynamics and lipolytic metabolic activity in response to external stimuli, a cell medium containing lipolytic agents, forskolin, and isoproterenol, was gently poured and mixed in the trans-well chamber over time. A combination of 20 μM forskolin and 5 μM triacsin was used to stimulate lipolysis⁴⁴ and prevent the regeneration of triglycerides⁴⁵. In contrast, 10 μM isoproterenol, acting through a different mechanism of cellular signaling⁴⁶, was used to stimulate lipolysis. Additionally, 5 μM verapamil was added to forskolin solution to check possible lipolytic change by blocking calcium (influx) channels⁴⁷ important for regulation of the lipid metabolism^{48,49}. For control samples, no lipolytic agents were added in the trans-well chamber. A 12-well plate with Transwell inserts was then transferred into the stage-top incubator (H301-K-FRAME, Okolab) mounted on an inverted microscope (Nikon ECLIPSE Ti2) for LD dynamics studies on live adipocytes. The experiment was run for a total of 6 to 24 hours, with lipolytic agents being added 2-3 hours after the start.

Optical setup. Adipocyte LDs, as natural intracellular optical microresonators, were excited at their circumference using a nanosecond pulsed (Opotek, OpoletteTM 355) and compact diode CW (Thorlabs) lasers, both set to a wavelength of $\lambda = 532 \text{ nm}$, optimized for BODIPY laser dye excitation. For the optimal lasing on live adipocytes, the typical energy per pulse of the pulsed laser with a 20 Hz repetition rate was 0.1-0.5 μJ (irradiance $E_e < 10^9 \text{ W/cm}^2$), and the power of the CW laser was 0.1 μW with irradiance $E_e \approx 10 \text{ W/cm}^2$. The lasers were aligned in the back port of the microscope. For optimal focusing and detection of WGM resonances, a 20 \times objective ($NA = 0.45$) and exposure times of 0.5 to 5 seconds were used, respectively. WGM spectra were captured using an imaging spectrometer (Shamrock SR-500i, Andor) with a diffraction grating of 1.200 lines per millimeter, resulting in a resolution of 0.07 nm. A 50 μm wide slit aperture was used at the spectrometer entrance for optimal confocality and signal-to-noise (S/N). Wide-field fluorescence imaging of cell organelles, LDs, plasma membrane, and nuclei was acquired simultaneously in separate fluorescence channels with a digital camera

(sCMOS Zyla 4.2, Andor) using LED source illumination (CoolLED, pE-300 white), dichroics and band-pass filters (all Semrock).

Image/spectral analysis. The measured spectra of pump-induced lasing or high S/NASE are the superposition of (differently polarized) transverse electric (TE) and/or transverse magnetic (TM) spectral eigenmodes/WGMs³. Their positions were calculated according to the first order radial modes approximation description^{50,51}, where each peak position was fitted with the following function:

$$L(\lambda) = \sum_{i_{TM}, i_{TE}} \frac{1}{2\pi} \frac{\Gamma}{(\lambda - \lambda_{i_{TM}, i_{TE}})^2 + (1/2\Gamma)^2}. \quad (1)$$

$\lambda_{i_{TM}, i_{TE}}$ are the spectral peak positions of individual eigenmode functions, and Γ is a parameter specifying function width. The example of spectral fits to the background-subtracted and normalized raw data (Figure S1a) in a time experiment is shown in Figure S1b. In cases of low S/N ASE, where the spectra resembled a sinusoidal shape, we developed an empirical model that nicely fits the experimental data after removing the background signal. Such broadened spectra are typical for a large number of measured adipocytes with non-complete sphericity and smoothness of the LD surface. The corresponding empirical model is:

$$f(\lambda) = A \sin[(k(1 - B(\lambda - \lambda_{min})^2)\lambda + \phi)] \quad (2)$$

where A is the intensity of the WGM peaks, k is the wavenumber of the quasi-sinusoidal function at the left boundary of the measured spectral interval at λ_{min} and ϕ is the phase shift required to properly align the fitting function to the measured WGM resonances. B is the scaling constant to properly fit the nonlinear (quadratic) dependence of the spacing between consecutive resonant modes, the so-called free spectral range (FSR), with wavelength λ . B can be used to extract the refractive index dispersion with the wavelength $\Delta n(\lambda)$. Due to typically smaller $\Delta n(\lambda)$ than the measured peak position uncertainty in low S/N spectra obtained in multiple cases, we simplified the model. Since the wavenumber k is inversely proportional to FSR ($k \propto 1/\text{FSR}$) and FSR is proportional to the square of wavelength ($\text{FSR} \propto \lambda^2$), one can adapt the model into:

$$f(\lambda) = A \sin[k'\lambda^{-1}] \quad (3)$$

where $k' \propto 2\pi n_{\text{eff}} R$ is the effective wavenumber, n_{eff} is the effective refractive index of LD influenced by the surrounding medium through the evanescent field and R is the LD radius. Once fitted, whether by equation 1, in case of high WGMs Q-factor ($>10^3$) (Figure S2a), or equations 2 and 3, in case of low WGMs Q-factor ($<10^3$) (Figure S2b), the sequential spectral fits of the optimized raw data in the time experiment were cross-correlated (Figure S1c) to quantify the spectral shift ($\Delta\lambda_{TM, TE}$) and hence the size change of adipocyte LD (Δd) assuming a few assumptions presented in Results and discussion section. Given the uncertainty in peak position determination we can also quantify the precision/resolution of the LD size.

3. Results and discussion

3.1. Experimental approach for nanometer-precision optical sensing of mature adipocytes

Adipocytes isolated from mouse or human adipose tissue represent one of the most challenging biological systems for advanced microscopy techniques. Their study requires careful optimization of both experimental conditions and optical sensing to capture fast, dynamic processes. The unique properties of adipocytes—particularly their highly spherical shape and low density—contribute to their buoyancy in the cellular medium, necessitating a customized imaging platform, as previously demonstrated⁵². On one hand, their near-perfect sphericity demands three-dimensional fluorescence imaging for accurate characterization of cell morphology and, critically, cell viability. On the other hand, their buoyancy and surface confinement require an optimized experimental setup, achieved here using a translucent ceiling trans-well system (schematic in Figure 1a). This workflow enabled controlled administration of chemical reagents to stimulate metabolic activity while maintaining the immobility of non-adherent, mature adipocytes—essential for dynamic single-cell studies. We began with large-field-of-view (FoV) bright-field (BF) imaging to assess the quality of adipocyte isolation, evaluate ceiling coverage under the trans-well, and determine cell size distribution (Figures 1 and 2a). Evenly distributed pores, averaging 8 μm in diameter and visible in fluorescence imaging (see arrows), facilitated solvent diffusion from the top to the bottom chamber, achieving complete mixing and concentration equalization within one hour (Figure S3). Finally, fluorescently labeled LDs were illuminated at their circumference with a laser to excite WGMs (Figure 1c).

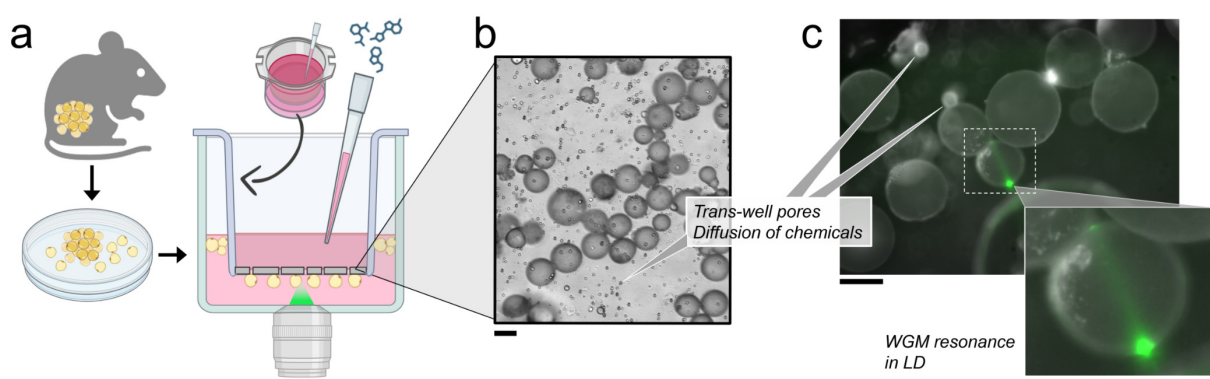


Figure 1. Trans-well-based experimental setup with the typical size, surface coverage, and localized optical resonance in mature adipocytes isolated from mice. (a) Schematics of a workflow and a translucent trans-well insert placed in a 12-well plate where the cells are homogeneously distributed under the surface. The plate was mounted on a stage top incubator fitted on an inverted microscope. (b) A typical example of a bright field (BF) image, showing cell distribution and size with visible 8 μm pores that enable diffusion and exchange of chemicals between the upper and lower chambers. (c) An

example of a fluorescence image of adipocytes with the locally focused laser beam (in green) exciting WGM resonances in a vertical plane visible as a line and a smaller bright spot on the other side of the LD. Scale bar is 50 μm .

Prior to measuring LD size via optical resonances, we assessed adipocyte viability using plasma membrane staining (CellMask Deep Red) and nucleic acid staining (SYTOX Deep Red), enabling both direct and indirect detection of compromised membranes (Figure 2b). Variability in sample preservation across biological replicates—likely due to differences in AT from individual mice—resulted in adipocyte viability ranging from approximately 50% to 80% (Figure S4). Fluorescence staining also allowed us to evaluate the functional integrity and structural changes of adipocytes. The results presented in Figure S5 suggest potential cellular mechanisms involving plasma membrane remodeling, discussed in greater detail in Supplementary Note A. Given the complexity of the biological system under study, we focused exclusively on mature, non-differentiated adipocytes that maintained structural and functional integrity of both the plasma membrane and LDs throughout the duration of the experiment.

3.2. Biological assessment and evaluation of LD lasing

By precisely positioning the pump laser at the perimeter of LDs, we excited the gain medium composed of Bodipy-based Pyromethene 597 (Figure 2c). The resulting fluorescent light was confined along the LD boundary via total internal reflection, as illustrated schematically in Figure 2d, producing distinct spectral features known as WGMs (Figure 2e and Supplementary Video 1). Depending on the excitation source—pulsed or continuous-wave (CW) laser—different gain conditions were achieved, resulting in either true lasing or cavity-modified fluorescence⁵. In both cases, the spectra exhibited sharp lines corresponding to WGM resonances; however, under lasing conditions, these lines were narrower and more pronounced (Figure 2e, right panel). Surpassing the lasing threshold required high concentrations of the lipophilic fluorescent dye and particularly high-energy nanosecond pulsed laser excitation, reaching up to μJ per pulse. These settings were found to induce local photodamage in adipocytes via photoablation, as detailed in reference⁵³. High-Q WGMs below the damage threshold were only achievable in adipocytes with structurally compromised LDs that exhibited near-perfect sphericity. This geometry, along with a smooth and polished LD surface, is known to support sharp resonance peaks⁵⁴ and enable sub-nanometer resolution¹⁴. In practice, however, the shape and surface smoothness of LDs are influenced by mechanical and tension forces exerted by the surrounding cytoskeleton—primarily a diffuse

cortical actin network⁵⁵ and intermediate/vimentin filaments⁵⁶. These forces can locally disrupt LD sphericity and surface integrity, significantly reducing the achievable Q-factor.

In fact, only a small number of adipocytes emitted measurable WGMs when excited with nanosecond pulsed laser light at power levels below the damage threshold. Surprisingly, a cost-effective, low-power CW diode laser outperformed the pulsed laser in both spectral sensitivity and safety, as demonstrated on the same adipocyte (Figure S6). We identified the CW diode laser as the only light source suitable for 100% safe WGM-based biosensing in native, mature adipocytes. Its operating parameters—carefully set just below the threshold for photochemical or photothermal effects (Figure S6, inset schematic)—consistently produced detectable WGMs. The SNR varied depending on the concentration of the gain medium and local deviations in sphericity and surface smoothness at the LD boundary of individual adipocytes (Figure 2e, left spectra; Figure S2).

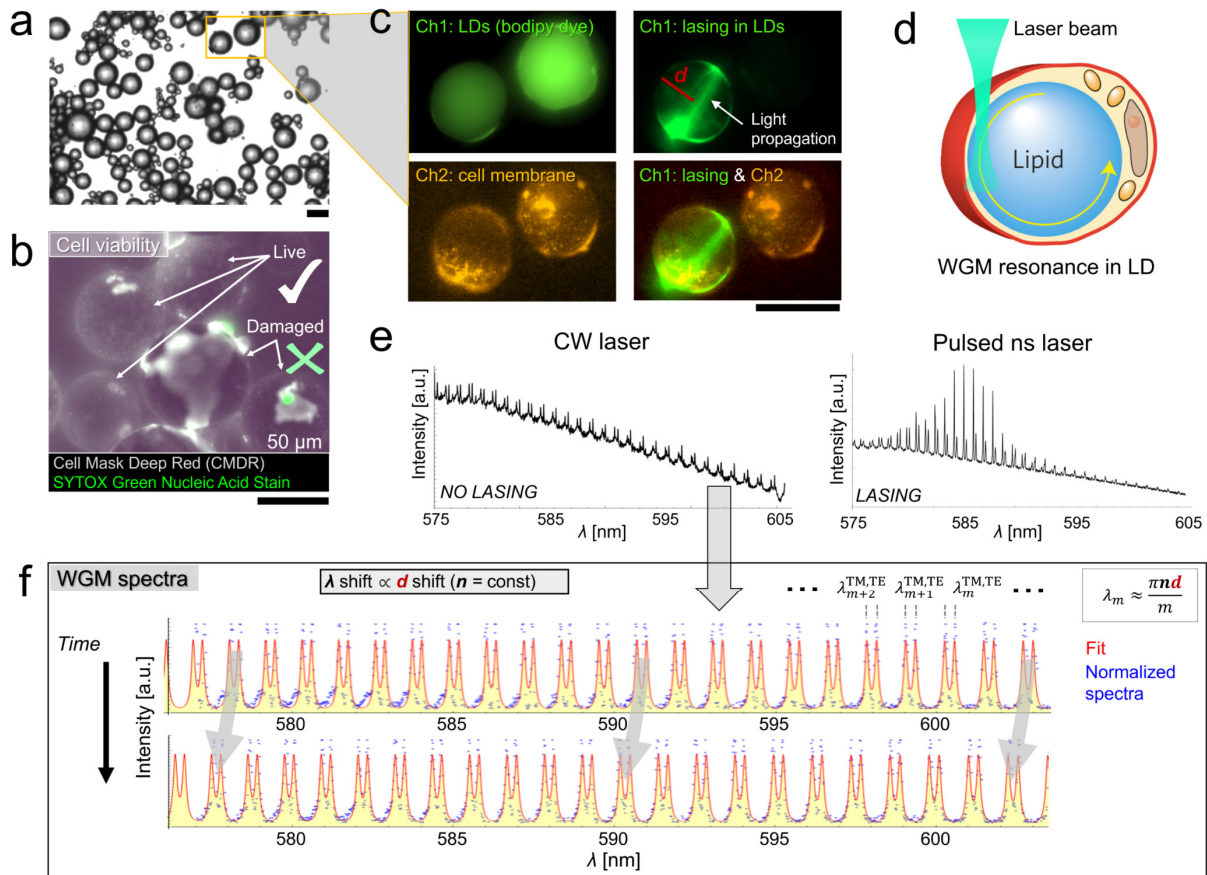


Figure 2. Typical images of adipocytes and excitation of WGMs and their spectra for ultraprecise dynamics study. (a) Bright field (BF) image of isolated adipocytes. (b) An example of cell viability measurement with double staining used to evaluate both structural and functional integrity. Typically, damaged cells with the labeled nuclei (in green) are accompanied by ruptured cell membranes (more images in Figure S4b and the Supplementary Video 2). (c) Upper row: fluorescence of LDs and CW laser-induced light propagation at the LD circumference observed in the same channel (Ch1, in green). Bottom row: fluorescence of cell plasma membrane observed in other channel (Ch2, in orange) and the

overlay of Ch1 - lasing and Ch2. (d) Schematics of the laser excitation of the dye within the LD and the light circulation at the LD circumference forming WGM resonances (adapted from ¹⁴). (e) Typical WGM spectra formed inside adipocyte LDs induced by CW laser (on the left) and pulsed ns laser (on the right). (f) The following analysis of WGM resonance spectra (points in blue) with typical transverse magnetic (TM) and transverse electric (TE) eigenmodes, to quantify the spectral peaks (λ_m) and hence the LD size (d) by using proper fitting (in red). Scale bar is 50 μm .

We acquired and analyzed WGM resonances induced by a CW laser. Spectra with higher SNR, exhibiting clearly distinguishable TM and TE spectral eigenmodes (Figure 2e, left panel; Figure 2f; Figure S2a), were fitted using the first-order radial mode approximation ⁵⁰. In contrast, spectra with lower SNR and significant spectral broadening (Figure S2b) were fitted using an empirical model, as detailed in the Materials and Methods section. Due to the lower Q-factor of the detected eigenmodes in both cases—compared to the high-Q WGM lasing spectra typically observed in embedded microspherical resonators—we could not match the maximal precision of 0.05 nm previously reported ¹⁴. However, by applying spectral fitting to eigenmodes with profiles resembling Gaussian shapes, and using a well-defined model for peak position error (dependent on spectrometer resolution, sampling density, and SNR) ⁵⁷ we calculated the uncertainty ($\sigma_{\lambda_{i_{TM},i_{TE}}}$) ⁵⁸, and thereby the resolution in peak position. This uncertainty is expressed by the following equation:

$$\sigma_{\lambda_{i_{TM},i_{TE}}} = \frac{\sqrt{\Delta\lambda_s W}}{\text{SNR}} \sqrt{\frac{\Delta}{F(\Lambda)}}, \quad (4)$$

where $\Delta\lambda_s$ is the wavelength sampling step ($\Delta\lambda_s = 0.02$ nm); W is related to the spectral full width at half maximum (FWHM; w) as $W \approx w/2.35$; SNR is defined as the maximum signal value at each eigenmode divided by the spectral noise; Δ is a numerical constant representing the confidence limit for a one-parameter fit ($\Delta = 1$ corresponding to a 68% confidence interval or "1 σ " error); $F(\Lambda)$ is a dimensionless factor derived from the integral of $(\partial S_{\text{eigenmode}}/\partial \lambda_{i_{TM},i_{TE}})^2$ over the λ -acquisition range (Λ), where $S_{\text{eigenmode}}$ denotes the spectral profile of the individual eigenmode. Given that our acquisition range spans the full spectrum, $F^{1/2}$ assumes a value of approximately 0.8 under the assumption of Gaussian noise ⁵⁷. Prior to calculating $\sigma_{\lambda_{i_{TM},i_{TE}}}$, the equation was slightly adjusted to account for oversampling in $\Delta\lambda_s$ relative to the spectrometer resolution (0.06 - 0.07 nm). This oversampling effectively reduced the number of independent data points across the acquisition range, leading to a modest increase in peak position uncertainty, as supported by analytical and numerical evaluations in study ⁵⁷. For the spectra shown in Figure 2f and Figure S2a—with an SNR of approximately 40 and $w \approx 0.15$ nm—the WGM peak uncertainty was calculated to be $\sigma_{\lambda_{i_{TM},i_{TE}}} \approx 0.005$ nm.

WGM resonance positions are sensitive to the changes of both size (d) and refractive index of the LD (n_{LD}) and the near surroundings inside cell cytoplasm (n_{cell}). Since the typical changes

in d measured by our methodology are more than 10^3 times smaller than the d itself, the composition of the molecules cannot change enough to cause any detectable variation in the n_{LD} . On the other hand, n_{cell} can vary more significantly over time, as indicated by its known spread across a population of cells ($\Delta n_{cell} \approx 0.0003$)⁵⁹. Since the variation of n_{cell} within a single cell is smaller than that observed across a population of physically and metabolically heterogeneous cells - and given that WGM resonances are considerably less sensitive to changes in n_{cell} than in n_{LD} - such a small Δn_{cell} is likely undetectable in our spectra. This makes Δd the primary cause of the measured spectral shifts.

In addition to Δd , spectral shifts may also arise from local deviations of the lipid droplet (LD) from perfect sphericity, potentially coupled with cellular rotation between consecutive time points. To assess such deviations, we analyzed LD size at various points along its circumference by altering the lasing position (Figure S7). The observed dispersion in LD size, $\Delta d \approx 10\text{nm}$, measured across multiple cells, was smaller than the typical spectral changes recorded during time-lapse experiments following drug administration/external stimuli (Figure 3). Therefore, morphological heterogeneity is expected to have minimal impact on the accuracy of quantifying biological heterogeneity and LD dynamics over hour-scale observations. Nonetheless, it is essential to carefully account for these factors.

To estimate the achievable repeatability in the measured d , it is necessary to account for potential scatter and noise in the multiple spectra acquired from a stable LD during a typical time-lapse experiment. WGM spectra recorded over a 3-hour interval with 0.5-hour time steps on a stable LD (Figure S8) revealed minimal peak scatter, approximately $w_s = 0.04\text{ nm}$ (FWHM, Figure S8c), with a slight directional trend (red shift, Figure S8b), as discussed in Supplementary Note B. Since the observed scatter w_s slightly exceeds the WGM peak uncertainties from spectral fitting, $\sigma_{\lambda_{TM,TE}}$, we used w_s to estimate the achievable uncertainty of the measured Δd . Applying the relation $(\Delta d)_{min} = d w_s / \lambda$, we obtained an uncertainty—and thus a resolution—of approximately 3.5 nm, which is two orders of magnitude better than what is achievable with best confocal microscopy settings.

Our newly developed approach for ultraprecise quantification of LD size in individual adipocytes enables a range of time-resolved experiments to investigate adipocyte dynamics. These include sensing cellular state, detecting rapid metabolic fluctuations, and assessing functional heterogeneity following the administration of cellular stress reagents or any external stimuli that mimic relevant metabolic or disease conditions—all at the single-cell level. Initial results are demonstrated using isolated murine adipocytes.

3.3. Adipocyte heterogeneity and rapid metabolic response revealed by the rate of LD size change

Having demonstrated the ability to accurately quantify LD size, we now apply this capability to investigate the temporal dynamics of adipocytes. Specifically, we monitor LD size over time and evaluate its response to lipolytic stimulation with agents such as forskolin and isoproterenol.

The initial time points reveal heterogeneous behavior among individual mature adipocytes even prior to stimulation (Figure 3). Some cells exhibit an increase in LD size, others undergo lipolysis (a decrease in LD size), while the remainder maintain a steady-state (homeostatic) condition. Capturing multiple baseline time points before administering the lipolytic agent was essential for establishing a reference, enabling reliable quantification of LD kinetics following stimulation. The sparse and variable response to external stimuli reflects diverse and uneven activation across the cell population. Analysis of LD size dynamics/change (Δd) in stimulated adipocytes (Figure 3, left graphs) shows a slightly broader distribution skewed toward lipolysis. Given the inherent heterogeneity observed even in control samples, additional measurements are needed to assess the statistical significance of differences in LD size and, by extension, metabolic activity between exposed and non-exposed cells. Nevertheless, in nearly all biological replicates—each comprising approximately 10 adipocytes—we observed individual cases within the stimulated group showing substantial and rapid Δd across consecutive time points (Figure 3, asterisks; Figure S9, arrows). Notably, an increased rate of LD size change ($\Delta d/t$) was observed within a ~30-minute interval (Figure 3, right graphs).

Stimulation with isoproterenol (Figures 3a and b) resulted in a statistically significant increase in the population mean of the $\Delta d/t$. In contrast, stimulation with forskolin (Figure 3c) did not yield a significant difference in the population mean, but did reveal a significant increase in the variance of $\Delta d/t$. In treated cells, $\Delta d/t$ reached approximately 0.5 $\mu\text{m}/\text{h}$, compared to ~0.2 $\mu\text{m}/\text{h}$ in control cells. These findings provide a quantitative measure of the speed and extent of transient metabolic responses to lipolytic agents, highlighting a complex feedback mechanism that regulates both lipolysis and LD integrity. Among individual adipocyte responses, LD size varied by up to ± 200 nm within a 30-minute interval. From this, we estimated the molar flux of molecules involved in lipolysis and lipogenesis. For a 60 μm -sized adipocyte, the maximal molar flux—based on observed size changes—was calculated to be approximately 4×10^{-7} mol/m²/s. This corresponds to the transport of $\sim 10^9$ molecules/s across the LD surface, assuming an average triglyceride (TG) molecular volume of 2 nm³⁶⁰. To contextualize these results, the estimated molar flux is comparable to that reported in a recent study using a conventional lipolytic calorimetric assay on primary adipocytes⁶¹. In that study, a lipolytic rate of 160 nmol/well/h—assuming the total LD surface area in confluent cells approximates the surface area of the assay well—corresponds to a molar flux of 1.3×10^{-7} mol/m²/s. In Figure

3d, we present another applicability of our methodology for ultraprecise sensing of stimulated adipocyte metabolism using a combination of drugs. Forskolin and verapamil (in green) appear to exert a greater effect on lipolysis and its rate than forskolin alone (in blue). Verapamil may enhance forskolin-induced lipolysis indirectly by blocking calcium (Ca^{2+}) influx channels⁶². Reduced intracellular Ca^{2+} levels help sustain cAMP activity, which is essential for lipolysis. Conversely, elevated Ca^{2+} concentrations are known to suppress cAMP signaling⁶³ and consequently inhibit lipolysis in adipocytes⁶⁴. Further biological replicates are needed to confirm the role of verapamil in this process.

Our new approach, employing non-phototoxic CW laser, provides a valuable enhancement to existing lipolytic assays by offering a faster, more precise, and cost-effective method for sensing adipocyte responses to lipolytic agents. A key advantage is its ability to quantify responses at the single-cell level, revealing biological heterogeneity and potential intercellular interactions that conventional techniques may overlook.

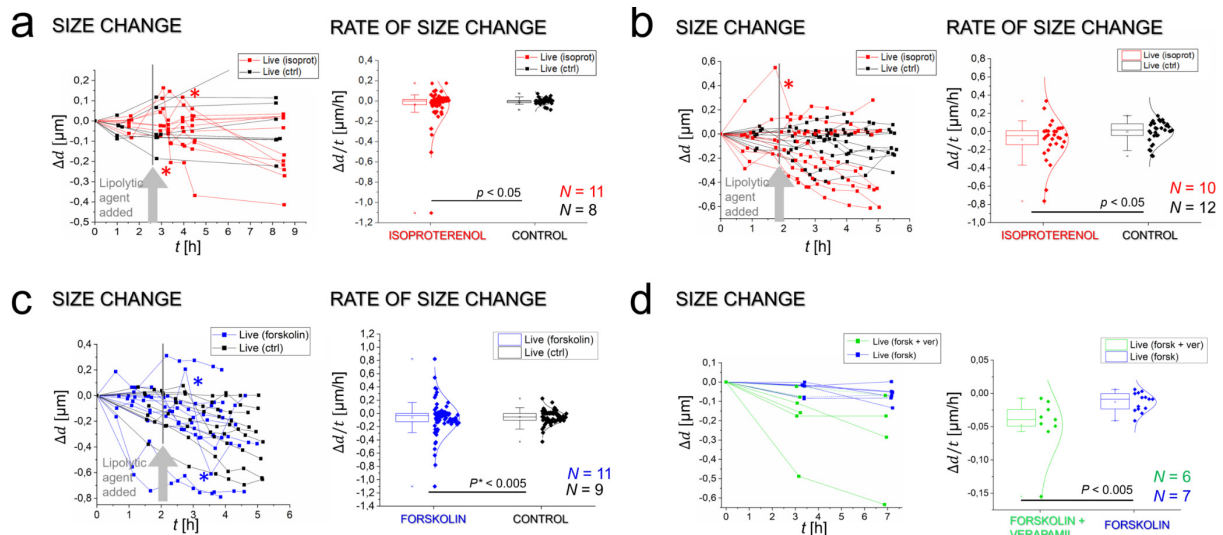


Figure 3. Measurements of LDs size dynamics to external stimuli introduced by isoproterenol and forskolin. (a) Isoproterenol-induced LDs size change (Δd) and LDs rate of size change ($\Delta d/t$) between consecutive time points performed on multiple cells over a longer time with a longer sampling interval. The results show significantly different population means ($p < 0.05$; two-sample t-test) of the $\Delta d/t$ between the exposed cells and the control. (b) Second biological replicate of isoproterenol-induced LDs Δd and $\Delta d/t$ performed on multiple cells over a shorter time with a shorter sampling interval. The results again show significantly different population means ($p < 0.05$) of the $\Delta d/t$ between the exposed cells and the control. (c) Results of forskolin-induced LDs Δd and $\Delta d/t$ performed on multiple cells in the time experiment. The results show significantly different population variance ($p^* < 0.005$; Levene's test used due to non-normal distribution of data) of the $\Delta d/t$ between the exposed cells and the control. (d) Results of verapamil-boostered LDs Δd and $\Delta d/t$ performed on multiple cells in the time experiment with long sampling interval. The results show significantly different population means ($p < 0.005$) of the $\Delta d/t$ between the cells exposed with the two and the control with one lipolytic agent.

3.4. WGM resonances enable fast diagnostics of cell viability

Throughout the study, fluorescence imaging revealed alterations in adipocyte plasma membrane morphology and integrity at the single-cell level (Figure 2b and S5). Interestingly, we noticed that these changes correlate with changes in the WGM resonances. A more detailed analysis (Figure 4) demonstrated that spectral changes occurred significantly earlier than those detectable by visual inspection or the SYTOX Deep Red viability assay. While CW laser was optimal for measuring metabolic activity in live adipocytes, we employed a pulsed laser in this context due to its superior sensitivity in distinguishing live from dead cells. To minimize potential photoablation damage, we used low laser doses and irradiances per pulse ($E_{\text{pulse}} < 500 \text{ nJ}$; $I_{\text{pulse}} < 10^9 \text{ W/cm}^2$), as shown in Figure S6.

As highlighted, WGM spectral analysis detected cellular damage prior to visual confirmation via fluorescence imaging—either directly through plasma membrane integrity (Figure 4a) or indirectly via nuclear staining (Figure 4b). Characteristic spectral transitions were observed as WGM resonances shifted from a non-lasing (sub-threshold) to a lasing mode (Figures 4a and b, blue to green spectra, indicated by the colored arrows). The full time-lapse sequence of adipocyte membrane rupture and partial LD release into the extracellular space for the example presented in Figure 4b is available in Supplementary Video 2.

WGM measurements are highly sensitive to ultrasmall changes in lipid droplet (LD) morphology, their physical properties, and the characteristics of the surrounding microenvironment. These measurements likely detect cytoskeletal remodeling—particularly actin and microtubule disruption—which precedes plasma membrane damage and eventual cell apoptosis. This underscores the importance of mechanical signals, alongside biological markers, in assessing cell viability, as recently demonstrated⁶⁵. A detailed spectral analysis (Figure 4c and Figure S10) revealed a subtle drift between the second and third time points, accompanied by a measurable increase in transverse electric (TE) and transverse magnetic (TM) mode splitting. This shift suggests a reduction in the refractive index of the LD's immediate surroundings (n_{cell}), primarily composed of cytoplasm. Spectral fitting indicated a decrease in Δn_{cell} of approximately 0.028 ± 0.002 , from $n_{\text{cell}} = 1.367$ to $n_{\text{cell}} = 1.339$, assuming $n_{\text{LD}} = 1.47$ ⁶⁶. These findings align with both spectral and visual evidence of compromised plasma membrane integrity, where cytoplasmic dilution due to extracellular fluid influx lowers n_{cell} . The increased mode splitting is likely attributable to the TM mode's heightened sensitivity to perturbations in the near-field environment, owing to its deeper penetration into the evanescent field at the resonator surface, as described in prior experimental and theoretical studies^{67,68}. Another example of this phenomenon is shown in Figure S11, where mode splitting correlates strongly with plasma membrane rupture. In this case, the refractive index of the cytoplasm decreased by $\Delta n = 0.032 \pm 0.002$, from approximately $n = 1.392$ to $n = 1.36$, indicating significant hydration and cytoplasmic loss. Through precise WGM spectral

quantification in adipocytes, this study not only captures rapid metabolic dynamics but also reveals the physiological state of cells prior to conventional viability assays.

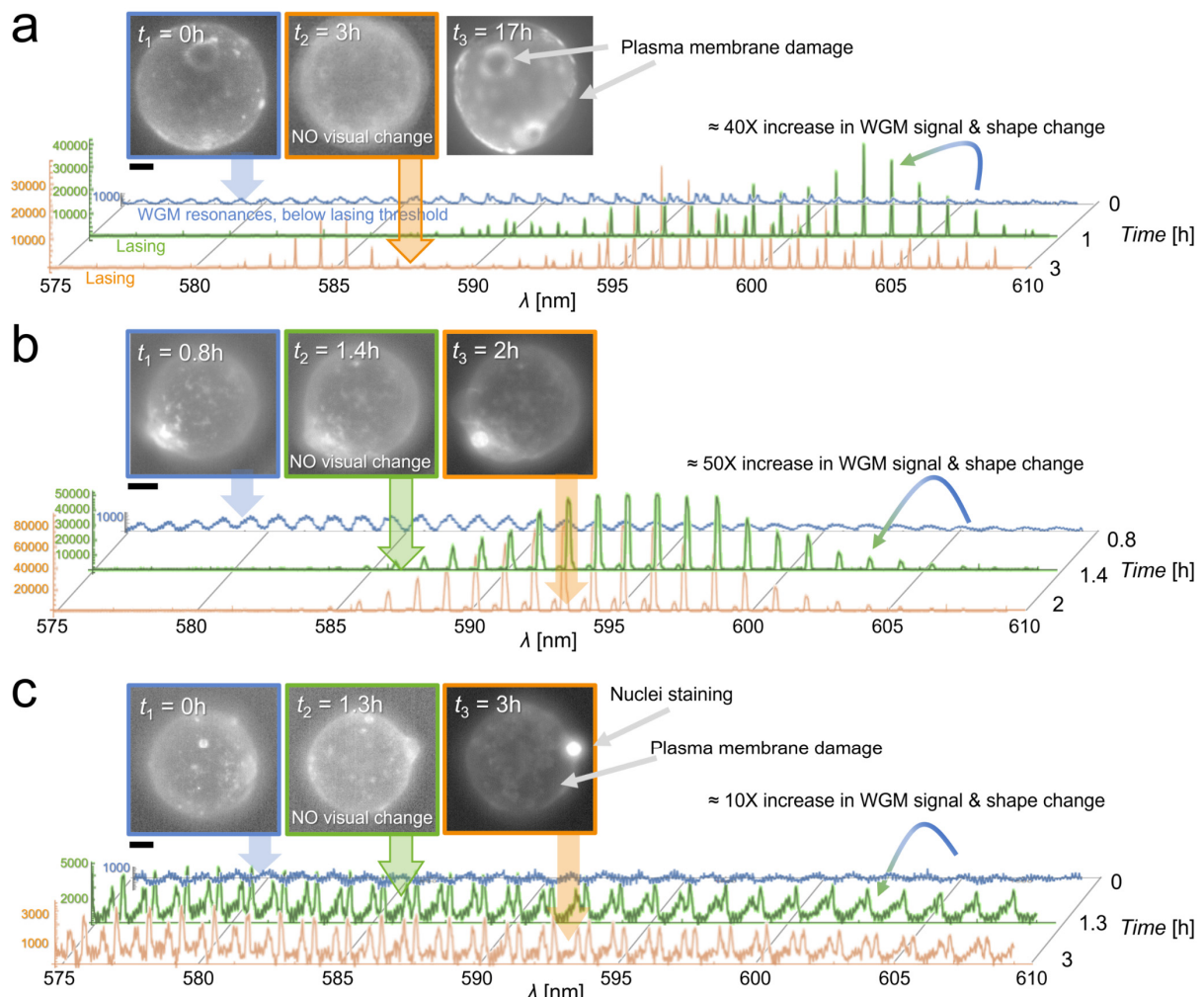


Figure 4. WGM spectra-based rapid diagnostics of adipocyte viability. (a) Fluorescence images of the same cell at three time points, stained with CellMask Deep Red and the corresponding lasing spectra color-coded in blue, green and orange. (b-c) Two more examples on other adipocytes which undergo plasma membrane rupture observed additionally with the nuclei staining viability assay. Again, spectral change observed between first and second time points was detected before any morphological change (image outlined in green) and before being diagnosed with the viability assay (image outlined in orange). The time-lapse of the adipocyte damage, including the excretion of LD content, is provided in the Supplementary Video 2. The scale bar is 10 μm .

Time-lapse experiments across multiple biological replicates also revealed that damaged cells—initially identified by spectral changes and later confirmed by plasma membrane disruption (Figure 4)—exhibited a loss of LD dynamics, maintaining a constant LD size over time (Figure 5). The distinction between damaged and viable adipocytes is clearly

demonstrated by comparing the distributions of LD size dynamics (black vs. orange). These findings reinforce that LD dynamics, monitored over several hours, serve as a reliable indicator of cellular state and viability.

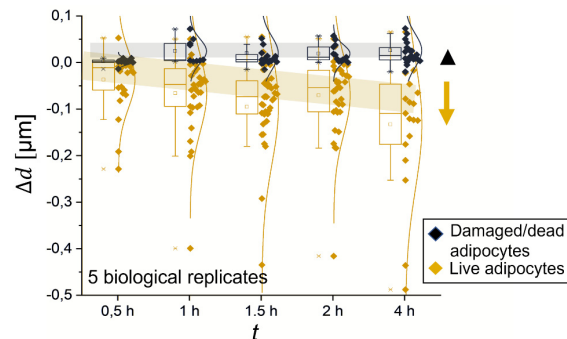


Figure 5. A comparison and a clear difference in the dynamics of LDs size change (Δd) between live and damaged adipocytes obtained from 5 biological replicates, each analyzing several cells. The sample size for each biological replicate was 5-10.

4. Conclusions and future outlook

We present a novel experimental methodology for precisely sensing adipocyte size dynamics with exceptionally high spatial (sub-nanometer) and temporal (sub-minute) resolution. This approach builds on our earlier study, where we demonstrated lasing inside live cells for the first time¹⁴. We systematically investigated the physical and biological aspects of photonic sensing in live, mature adipocytes, highlighting both its capabilities and limitations. Due to the non-spherical and uneven morphology of LDs in live adipocytes, conventional methods for generating WGM resonances proved inadequate. Instead of using a pulsed nanosecond laser—which requires high lasing powers and risks photo-induced damage—we implemented a cost-effective, low-power CW laser. Although this setup did not yield the maximum Q-factor or spectral resolution typical of pulsed lasers, it was not a limiting factor. The temporal spectral noise was comparable to the peak position uncertainty from spectral fitting, resulting in a precision of approximately 3.5 nm—two orders of magnitude better than the optical resolution achievable with confocal microscopy. Using precise WGM spectral characterization and appropriate fitting models, we quantified biological and morphological heterogeneity in adipocytes and captured rapid metabolic responses to external lipolytic stimuli. These responses were measurable through changes in LD size and molecular flux rates. Moreover, WGM spectral shifts proved to be a promising tool for rapid diagnostics of cellular state and viability. Our results establish a proof-of-concept that significantly enhances current lipolytic and viability assays by offering a faster, more cost-effective, and single-cell-level assessment of adipocyte heterogeneity. Unlike conventional assays, which rely on bulk cell populations and cannot resolve interactions between individual cells, our methodology

enables such analysis. If adapted for high-throughput and automated imaging, this approach holds broad potential for studying metabolism- and obesity-related diseases across cellular and tissue scales. It would substantially increase sample size and statistical power, improving precision in characterizing biological and morphological heterogeneity and enabling more robust insights into dynamic processes within adipose tissue.

Acknowledgement

This work was supported by the European Research Council (ERC) under the European Union's Horizon 2020 research and innovation program (ERC Starting Grant, GA851143) and by the Slovenian Research and Innovation agency (ARIS) (P1-0099, N1-0362 and P1-0140).

Authors Contributions

R.P. conducted and designed the experiments, analyzed the results and wrote the manuscript with input from other authors; A. K. prepared the designed the sample preparation; M.G.Z. conducted initial experiments; P.M.Š. prepared the samples; S.U. supported original idea and supervised the study; M. H. conceived the original idea, designed, and supervised the study.

5. References

- (1) Pan, T.; Lu, D.; Xin, H.; Li, B. Biophotonic Probes for Bio-Detection and Imaging. *Light Sci Appl* **2021**, *10* (1), 124. DOI: 10.1038/s41377-021-00561-2.
- (2) Foreman, M. R.; Swaim, J. D.; Vollmer, F. Whispering Gallery Mode Sensors. *Adv. Opt. Photon., AOP* **2015**, *7* (2), 168–240. DOI: 10.1364/AOP.7.000168.
- (3) Matsko, A. B.; Ilchenko, V. S. Optical Resonators with Whispering-Gallery Modes-Part I: Basics. *IEEE Journal of Selected Topics in Quantum Electronics* **2006**, *12* (1), 3–14. DOI: 10.1109/JSTQE.2005.862952.
- (4) Yu, D.; Humar, M.; Meserve, K.; Bailey, R. C.; Chormaic, S. N.; Vollmer, F. Whispering-Gallery-Mode Sensors for Biological and Physical Sensing. *Nat Rev Methods Primers* **2021**, *1* (1), 1–22. DOI: 10.1038/s43586-021-00079-2.
- (5) Humar, M. Liquid-Crystal-Droplet Optical Microcavities. *Liquid Crystals* **2016**, *43* (13–15), 1937–1950. DOI: 10.1080/02678292.2016.1221151.
- (6) Vollmer, F.; Yu, D. *Optical Whispering Gallery Modes for Biosensing: From Physical Principles to Applications*; Springer International Publishing: Cham, 2022. DOI: 10.1007/978-3-031-06858-4.
- (7) Cai, L.; Pan, J.; Zhao, Y.; Wang, J.; Xiao, S. Whispering Gallery Mode Optical Microresonators: Structures and Sensing Applications. *physica status solidi (a)* **2020**, *217* (6), 1900825. DOI: 10.1002/pssa.201900825.

- (8) Loyez, M.; Adolphson, M.; Liao, J.; Yang, L. From Whispering Gallery Mode Resonators to Biochemical Sensors. *ACS Sens.* **2023**, *8* (7), 2440–2470. DOI: 10.1021/acssensors.2c02876.
- (9) Fu, Y.; Lin, S.; Wang, X.-H. Whispering Gallery Mode Micro/Nanolasers for Intracellular Probing at Single Cell Resolution. *ACS Sens.* **2024**, *9* (11), 5683–5698. DOI: 10.1021/acssensors.4c01634.
- (10) Yu, W.; Jiang, W. C.; Lin, Q.; Lu, T. Cavity Optomechanical Spring Sensing of Single Molecules. *Nat Commun* **2016**, *7* (1), 12311. DOI: 10.1038/ncomms12311.
- (11) Baaske, M. D.; Foreman, M. R.; Vollmer, F. Single-Molecule Nucleic Acid Interactions Monitored on a Label-Free Microcavity Biosensor Platform. *Nat Nanotechnol* **2014**, *9* (11), 933–939. DOI: 10.1038/nnano.2014.180.
- (12) Vollmer, F.; Arnold, S. Whispering-Gallery-Mode Biosensing: Label-Free Detection down to Single Molecules. *Nat Methods* **2008**, *5* (7), 591–596. DOI: 10.1038/nmeth.1221.
- (13) Vollmer, F.; Arnold, S.; Keng, D. Single Virus Detection from the Reactive Shift of a Whispering-Gallery Mode. *Proceedings of the National Academy of Sciences* **2008**, *105* (52), 20701–20704. DOI: 10.1073/pnas.0808988106.
- (14) Humar, M.; Hyun Yun, S. Intracellular Microlasers. *Nature Photon* **2015**, *9* (9), 572–576. DOI: 10.1038/nphoton.2015.129.
- (15) Schubert, M.; Steude, A.; Liehm, P.; Kronenberg, N. M.; Karl, M.; Campbell, E. C.; Powis, S. J.; Gather, M. C. Lasing within Live Cells Containing Intracellular Optical Microresonators for Barcode-Type Cell Tagging and Tracking. *Nano Lett.* **2015**, *15* (8), 5647–5652. DOI: 10.1021/acs.nanolett.5b02491.
- (16) Humar, M.; Upadhyaya, A.; Yun, S. H. Spectral Reading of Optical Resonance-Encoded Cells in Microfluidics. *Lab Chip* **2017**, *17* (16), 2777–2784. DOI: 10.1039/C7LC00220C.
- (17) Kavčič, A.; Garvas, M.; Marinčič, M.; Unger, K.; Coclite, A. M.; Majaron, B.; Humar, M. Deep Tissue Localization and Sensing Using Optical Microcavity Probes. *Nat Commun* **2022**, *13* (1), 1269. DOI: 10.1038/s41467-022-28904-6.
- (18) Martino, N.; Kwok, S. J. J.; Liapis, A. C.; Forward, S.; Jang, H.; Kim, H.-M.; Wu, S. J.; Wu, J.; Dannenberg, P. H.; Jang, S.-J.; Lee, Y.-H.; Yun, S.-H. Wavelength-Encoded Laser Particles for Massively Multiplexed Cell Tagging. *Nat. Photonics* **2019**, *13* (10), 720–727. DOI: 10.1038/s41566-019-0489-0.
- (19) Anwar, A. R.; Mur, M.; Humar, M. Microcavity- and Microlaser-Based Optical Barcoding: A Review of Encoding Techniques and Applications. *ACS Photonics* **2023**, *10* (5), 1202–1224. DOI: 10.1021/acsp Photonics.2c01611.
- (20) Humar, M.; Yun, S. H. Whispering-Gallery-Mode Emission from Biological Luminescent Protein Microcavity Assemblies. *Optica* **2017**, *4* (2), 222–228. DOI: 10.1364/OPTICA.4.000222.
- (21) Schubert, M.; Woolfson, L.; Barnard, I. R. M.; Dorward, A. M.; Casement, B.; Morton, A.; Robertson, G. B.; Appleton, P. L.; Miles, G. B.; Tucker, C. S.; Pitt, S. J.; Gather, M. C. Monitoring Contractility in Cardiac Tissue with Cellular Resolution Using Biointegrated Microlasers. *Nat. Photonics* **2020**, *14* (7), 452–458. DOI: 10.1038/s41566-020-0631-z.

- (22) Wang, Y.; Lang, M. C.; Lu, J.; Suo, M.; Du, M.; Hou, Y.; Wang, X.-H.; Wang, P. Demonstration of Intracellular Real-Time Molecular Quantification via FRET-Enhanced Optical Microcavity. *Nat Commun* **2022**, *13* (1), 6685. DOI: 10.1038/s41467-022-34547-4.
- (23) Yang, H.; Galea, A.; Sytnyk, V.; Crossley, M. Controlling the Size of Lipid Droplets: Lipid and Protein Factors. *Current Opinion in Cell Biology* **2012**, *24* (4), 509–516. DOI: 10.1016/j.ceb.2012.05.012.
- (24) Thiam, A. R.; Farese Jr, R. V.; Walther, T. C. The Biophysics and Cell Biology of Lipid Droplets. *Nat Rev Mol Cell Biol* **2013**, *14* (12), 775–786. DOI: 10.1038/nrm3699.
- (25) Zadoorian, A.; Du, X.; Yang, H. Lipid Droplet Biogenesis and Functions in Health and Disease. *Nat Rev Endocrinol* **2023**, *19* (8), 443–459. DOI: 10.1038/s41574-023-00845-0.
- (26) Hinte, L. C.; Castellano-Castillo, D.; Ghosh, A.; Melrose, K.; Gasser, E.; Noé, F.; Massier, L.; Dong, H.; Sun, W.; Hoffmann, A.; Wolfrum, C.; Rydén, M.; Mejhert, N.; Blüher, M.; von Meyenn, F. Adipose Tissue Retains an Epigenetic Memory of Obesity after Weight Loss. *Nature* **2024**, *636* (8042), 457–465. DOI: 10.1038/s41586-024-08165-7.
- (27) Quail, D. F.; Dannenberg, A. J. The Obese Adipose Tissue Microenvironment in Cancer Development and Progression. *Nat Rev Endocrinol* **2019**, *15* (3), 139–154. DOI: 10.1038/s41574-018-0126-x.
- (28) Olzmann, J. A.; Carvalho, P. Dynamics and Functions of Lipid Droplets. *Nat Rev Mol Cell Biol* **2019**, *20* (3), 137–155. DOI: 10.1038/s41580-018-0085-z.
- (29) Langin, D. Adipose Tissue Lipolysis as a Metabolic Pathway to Define Pharmacological Strategies against Obesity and the Metabolic Syndrome. *Pharmacol Res* **2006**, *53* (6), 482–491. DOI: 10.1016/j.phrs.2006.03.009.
- (30) Jarc, E.; Petan, T. A Twist of FATE: Lipid Droplets and Inflammatory Lipid Mediators. *Biochimie* **2020**, *169*, 69–87. DOI: 10.1016/j.biochi.2019.11.016.
- (31) Lynes, M. D.; Tseng, Y.-H. Deciphering Adipose Tissue Heterogeneity. *Ann N Y Acad Sci* **2018**, *1411* (1), 5–20. DOI: 10.1111/nyas.13398.
- (32) Whytock, K. L.; Sun, Y.; Divoux, A.; Yu, G.; Smith, S. R.; Walsh, M. J.; Sparks, L. M. Single Cell Full-Length Transcriptome of Human Subcutaneous Adipose Tissue Reveals Unique and Heterogeneous Cell Populations. *iScience* **2022**, *25* (8), 104772. DOI: 10.1016/j.isci.2022.104772.
- (33) Schweiger, M.; Eichmann, T. O.; Taschler, U.; Zimmermann, R.; Zechner, R.; Lass, A. Chapter Ten - Measurement of Lipolysis. In *Methods in Enzymology*; MacDougald, O. A., Ed.; Methods of Adipose Tissue Biology, Part B; Academic Press, 2014; Vol. 538, pp 171–193. DOI: 10.1016/B978-0-12-800280-3.00010-4.
- (34) Tatenaka, Y.; Kato, H.; Ishiyama, M.; Sasamoto, K.; Shiga, M.; Nishitoh, H.; Ueno, Y. Monitoring Lipid Droplet Dynamics in Living Cells by Using Fluorescent Probes. *Biochemistry* **2019**, *58* (6), 499–503. DOI: 10.1021/acs.biochem.8b01071.
- (35) Paar, M.; Jüngst, C.; Steiner, N. A.; Magnes, C.; Sinner, F.; Kolb, D.; Lass, A.; Zimmermann, R.; Zumbusch, A.; Kohlwein, S. D.; Wolinski, H. Remodeling of Lipid Droplets during Lipolysis and Growth in Adipocytes*. *Journal of Biological Chemistry* **2012**, *287* (14), 11164–11173. DOI: 10.1074/jbc.M111.316794.

- (36) Fan, L.; Wang, X.; Zan, Q.; Fan, L.; Li, F.; Yang, Y.; Zhang, C.; Shuang, S.; Dong, C. Lipid Droplet-Specific Fluorescent Probe for In Vivo Visualization of Polarity in Fatty Liver, Inflammation, and Cancer Models. *Anal. Chem.* **2021**, *93* (22), 8019–8026. DOI: 10.1021/acs.analchem.1c01125.
- (37) Chen, T.; Yavuz, A.; Wang, M. C. Dissecting Lipid Droplet Biology with Coherent Raman Scattering Microscopy. *Journal of Cell Science* **2021**, *135* (5), jcs252353. DOI: 10.1242/jcs.252353.
- (38) Kim, H.; Oh, S.; Lee, S.; Lee, K. suk; Park, Y. Recent Advances in Label-Free Imaging and Quantification Techniques for the Study of Lipid Droplets in Cells. *Current Opinion in Cell Biology* **2024**, *87*, 102342. DOI: 10.1016/j.ccb.2024.102342.
- (39) Kislev, N.; Eidelheit, S.; Perlmutter, S.; Benayahu, D. How to Follow Lipid Droplets Dynamics during Adipocyte Metabolism. *Journal of Cellular Physiology* **2022**, *237* (11), 4157–4168. DOI: 10.1002/jcp.30857.
- (40) Ntziachristos, V.; Pleitez, M. A.; Aime, S.; Brindle, K. M. Emerging Technologies to Image Tissue Metabolism. *Cell Metab* **2019**, *29* (3), 518–538. DOI: 10.1016/j.cmet.2018.09.004.
- (41) Jeon, Y. G.; Kim, Y. Y.; Lee, G.; Kim, J. B. Physiological and Pathological Roles of Lipogenesis. *Nat Metab* **2023**, *5* (5), 735–759. DOI: 10.1038/s42255-023-00786-y.
- (42) Lass, A.; Zimmermann, R.; Oberer, M.; Zechner, R. Lipolysis – A Highly Regulated Multi-Enzyme Complex Mediates the Catabolism of Cellular Fat Stores. *Prog Lipid Res* **2011**, *50* (1–4), 14–27. DOI: 10.1016/j.plipres.2010.10.004.
- (43) Jüngst, C.; Klein, M.; Zumbusch, A. Long-Term Live Cell Microscopy Studies of Lipid Droplet Fusion Dynamics in Adipocytes[S]. *Journal of Lipid Research* **2013**, *54* (12), 3419–3429. DOI: 10.1194/jlr.M042515.
- (44) Okuda, H.; Morimoto, C.; Tsujita, T. Relationship between Cyclic AMP Production and Lipolysis Induced by Forskolin in Rat Fat Cells. *Journal of Lipid Research* **1992**, *33* (2), 225–231. DOI: 10.1016/S0022-2275(20)41542-1.
- (45) Baskaran, P.; Thyagarajan, B. Measurement of Basal and Forskolin-Stimulated Lipolysis in Inguinal Adipose Fat Pads. *J Vis Exp* **2017**, No. 125, 55625. DOI: 10.3791/55625.
- (46) Allen, D. O.; Ahmed, B.; Naseer, K. Relationships between Cyclic AMP Levels and Lipolysis in Fat Cells after Isoproterenol and Forskolin Stimulation. *J Pharmacol Exp Ther* **1986**, *238* (2), 659–664. DOI: 10.1016/S0022-3565(25)24915-1.
- (47) McGoon, M. D.; Vlietstra, R. E.; Holmes, D. R.; Osborn, J. E. The Clinical Use of Verapamil. *Mayo Clin Proc* **1982**, *57* (8), 495–510.
- (48) Maus, M.; Cuk, M.; Patel, B.; Lian, J.; Ouimet, M.; Kaufmann, U.; Yang, J.; Horvath, R.; Hornig-Do, H.-T.; Chrzanowska-Lightowlers, Z. M.; Moore, K. J.; Cuervo, A. M.; Feske, S. Store-Operated Ca²⁺ Entry Controls Induction of Lipolysis and the Transcriptional Reprogramming to Lipid Metabolism. *Cell Metabolism* **2017**, *25* (3), 698–712. DOI: 10.1016/j.cmet.2016.12.021.
- (49) Song, Z.; Wang, Y.; Zhang, F.; Yao, F.; Sun, C. Calcium Signaling Pathways: Key Pathways in the Regulation of Obesity. *International Journal of Molecular Sciences* **2019**, *20* (11), 2768. DOI: 10.3390/ijms20112768.
- (50) Pang, S.; Beckham, R. E.; Meissner, K. E. Quantum Dot-Embedded Microspheres for Remote Refractive Index Sensing. *Applied Physics Letters* **2008**, *92* (22), 221108. DOI: 10.1063/1.2937209.

- (51) Lam, C. C.; Leung, P. T.; Young, K. Explicit Asymptotic Formulas for the Positions, Widths, and Strengths of Resonances in Mie Scattering. *J. Opt. Soc. Am. B, JOSAB* **1992**, *9* (9), 1585–1592. DOI: 10.1364/JOSAB.9.001585.
- (52) Kim, J.; Park, K.-Y.; Choi, S.; Ko, U. H.; Lim, D.-S.; Suh, J. M.; Shin, J. H. Ceiling Culture Chip Reveals Dynamic Lipid Droplet Transport during Adipocyte Dedifferentiation via Actin Remodeling. *Lab Chip* **2022**, *22* (20), 3920–3932. DOI: 10.1039/D2LC00428C.
- (53) Keiser, G. Light-Tissue Interactions. In *Biophotonics: Concepts to Applications*; Keiser, G., Ed.; Springer Nature: Singapore, 2022; pp 169–221. DOI: 10.1007/978-981-19-3482-7_6.
- (54) Toropov, N.; Cabello, G.; Serrano, M. P.; Gutha, R. R.; Rafti, M.; Vollmer, F. Review of Biosensing with Whispering-Gallery Mode Lasers. *Light Sci Appl* **2021**, *10* (1), 42. DOI: 10.1038/s41377-021-00471-3.
- (55) Potolitsyna, E.; Pickering, S. H.; Bellanger, A.; Germier, T.; Collas, P.; Briand, N. Cytoskeletal Rearrangement Precedes Nucleolar Remodeling during Adipogenesis. *Commun Biol* **2024**, *7* (1), 458. DOI: 10.1038/s42003-024-06153-1.
- (56) Heid, H.; Rickelt, S.; Zimbelmann, R.; Winter, S.; Schumacher, H.; Dörflinger, Y.; Kuhn, C.; Franke, W. W. On the Formation of Lipid Droplets in Human Adipocytes: The Organization of the Perilipin-Vimentin Cortex. *PLoS One* **2014**, *9* (2), e90386. DOI: 10.1371/journal.pone.0090386.
- (57) Bobroff, N. Position Measurement with a Resolution and Noise-limited Instrument. *Review of Scientific Instruments* **1986**, *57* (6), 1152–1157. DOI: 10.1063/1.1138619.
- (58) Urbančič, I.; Arsov, Z.; Ljubetič, A.; Biglino, D.; Strancar, J. Bleaching-Corrected Fluorescence Microspectroscopy with Nanometer Peak Position Resolution. *Opt Express* **2013**, *21* (21), 25291–25306. DOI: 10.1364/OE.21.025291.
- (59) Baczewska, M.; Eder, K.; Ketelhut, S.; Kemper, B.; Kujawińska, M. Refractive Index Changes of Cells and Cellular Compartments Upon Paraformaldehyde Fixation Acquired by Tomographic Phase Microscopy. *Cytometry Part A* **2021**, *99* (4), 388–398. DOI: 10.1002/cyto.a.24229.
- (60) Kim, S.; Swanson, J. M. J.; Voth, G. A. Computational Studies of Lipid Droplets. *J Phys Chem B* **2022**, *126* (11), 2145–2154. DOI: 10.1021/acs.jpcc.2c00292.
- (61) Bridge-Comer, P. E.; Reilly, S. M. Measuring the Rate of Lipolysis in Ex Vivo Murine Adipose Tissue and Primary Preadipocytes Differentiated In Vitro. *J Vis Exp* **2023**, No. 193, 10.3791/65106. DOI: 10.3791/65106.
- (62) Lee, K. S.; Tsien, R. W. Mechanism of Calcium Channel Blockade by Verapamil, D600, Diltiazem and Nitrendipine in Single Dialysed Heart Cells. *Nature* **1983**, *302* (5911), 790–794. DOI: 10.1038/302790a0.
- (63) DeBernardi, M. A.; Seki, T.; Brooker, G. Inhibition of cAMP Accumulation by Intracellular Calcium Mobilization in C6-2B Cells Stably Transfected with Substance K Receptor cDNA. *Proceedings of the National Academy of Sciences* **1991**, *88* (20), 9257–9261. DOI: 10.1073/pnas.88.20.9257.
- (64) Carmen, G.-Y.; Víctor, S.-M. Signalling Mechanisms Regulating Lipolysis. *Cell Signal* **2006**, *18* (4), 401–408. DOI: 10.1016/j.cellsig.2005.08.009.

- (65) Su, X.; Zhang, L.; Kang, H.; Zhang, B.; Bao, G.; Wang, J. Mechanical, Nanomorphological and Biological Reconstruction of Early-stage Apoptosis in HeLa Cells Induced by Cytochalasin B. *Oncol Rep* **2019**, *41* (2), 928–938. DOI: 10.3892/or.2018.6921.
- (66) Yanina, I. Y.; Lazareva, E. N.; Tuchin, V. V. Refractive Index of Adipose Tissue and Lipid Droplet Measured in Wide Spectral and Temperature Ranges. *Appl. Opt., AO* **2018**, *57* (17), 4839–4848. DOI: 10.1364/AO.57.004839.
- (67) Francois, A.; Himmelhaus, M. Optical Sensors Based on Whispering Gallery Modes in Fluorescent Microbeads: Size Dependence and Influence of Substrate. *Sensors* **2009**, *9* (9), 6836–6852. DOI: 10.3390/s90906836.
- (68) Teraoka, I.; Arnold, S.; Vollmer, F. Perturbation Approach to Resonance Shifts of Whispering-Gallery Modes in a Dielectric Microsphere as a Probe of a Surrounding Medium. *J. Opt. Soc. Am. B, JOSAB* **2003**, *20* (9), 1937–1946. DOI: 10.1364/JOSAB.20.001937.

Supplementary Data

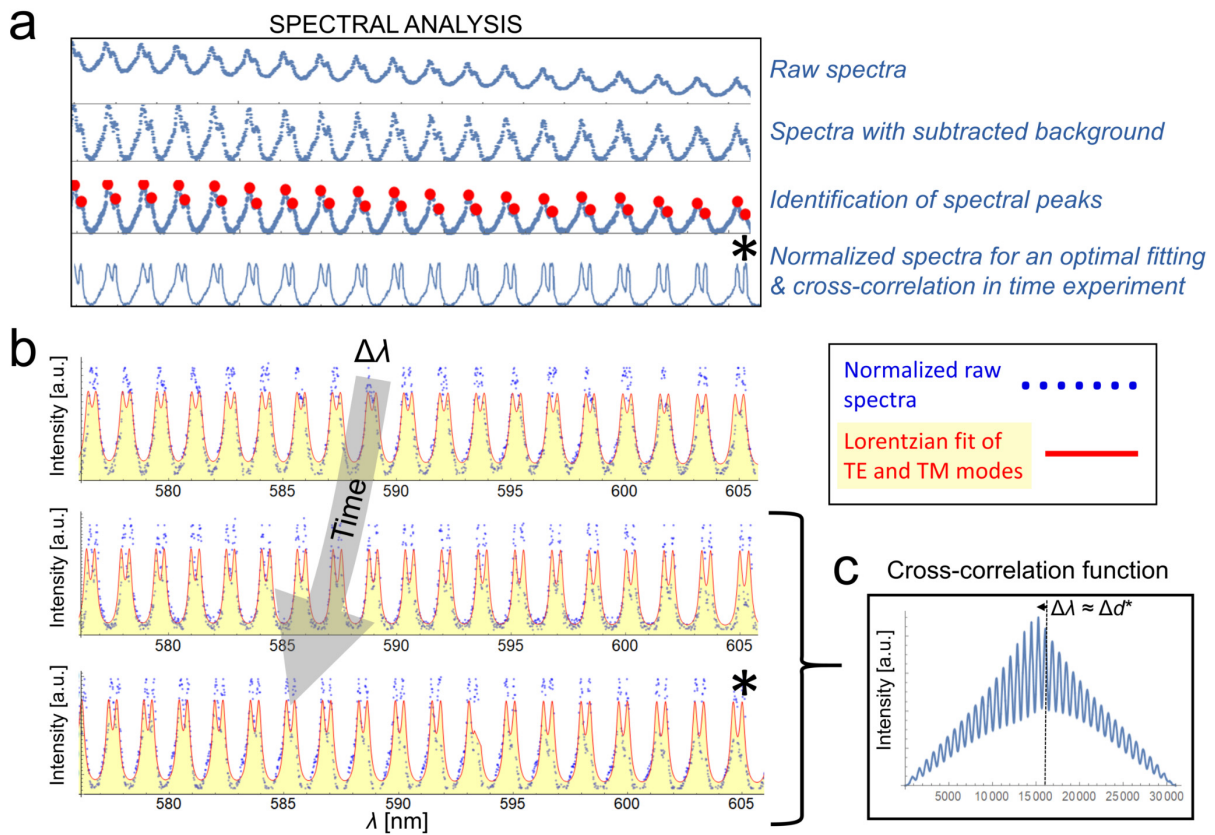


Figure S1. Consecutive steps of the LDs WGMs spectra analysis. (a) Spectra preparation for the optimized fitting. (b) Fitting of normalized spectra by using first order radial mode approximation description and Lorentzian function for TE and TM eigenmodes. (c) Cross-correlation of the sequential fits to quantify the spectral shift $\Delta\lambda$ and the related adipocyte size change Δd in the time experiment. The calculation of Δd is valid for the constant refractive index of the surrounding cell cytoplasm with time. Exemplary data for spectral analysis shown in (a) is taken from the data from the last time point of the dynamics experiment shown in (c), as denoted with an asterisk. A spectral blue shift with time is marked with a gray arrow.

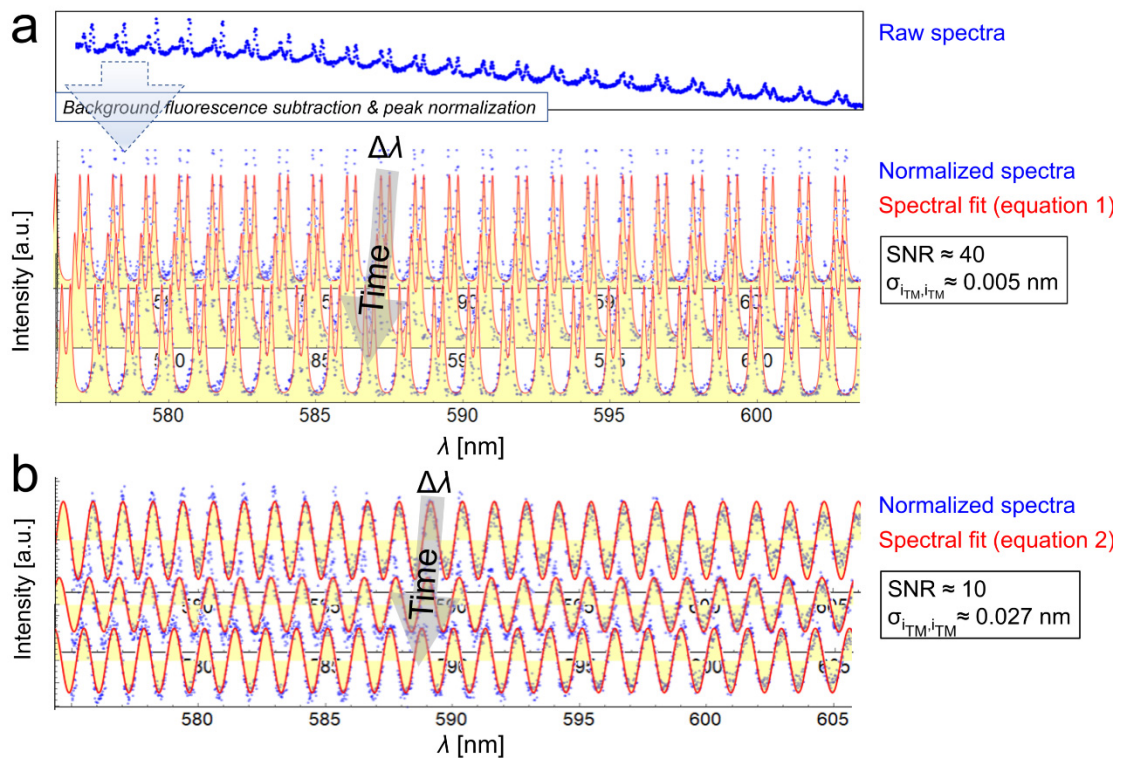


Figure S2. An example of different spectral fits to differently-shaped, background-subtracted and normalized raw WGM spectral data in a time experiment. (a) The workflow for precise spectral fitting and analysis of distinctly observed TM and TE eigenmodes providing the spectral peak uncertainty of $\sigma_{i_{TM},i_{TM}} \approx 0.005$ nm for ultraprecise characterization of adipocyte size. (b) Precise spectral fitting and analysis of the WGM spectra with an extensive spectral broadening providing the spectral peak uncertainty of $\sigma_{i_{TM},i_{TM}} \approx 0.027$ nm.

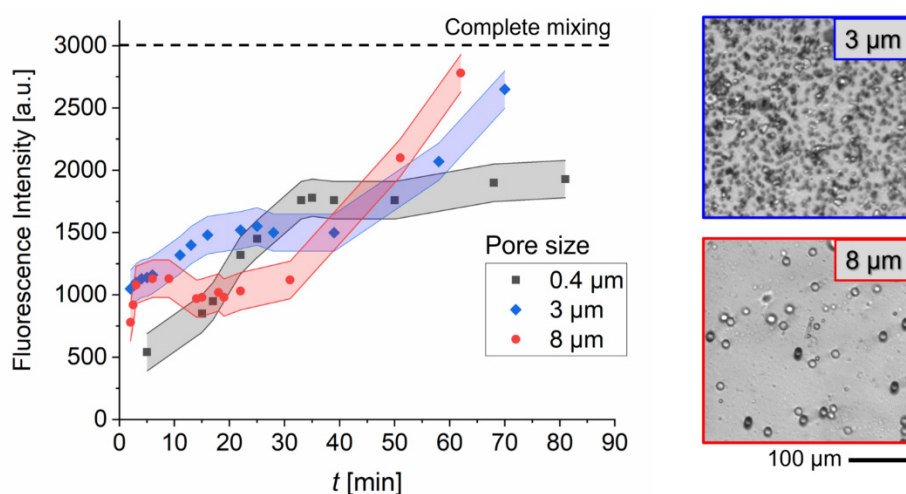


Figure S3. Diffusive transport of small molecules through different-sized pores in a trans-well system to reach complete mixing between both chambers. Faster transport of molecules through smaller 3 μm pores as compared to 8 μm pores in the first 30 min is attributed to the

much higher density of smaller pores, as seen in the right images. The Trans-well with the smallest pores (0.4 μm in gray) did not achieve complete mixing within 90 minutes and was thus not used in our study. On the other side, both 3 μm and 8 μm trans-well chambers were appropriate for our multi-hour dynamics study on adipocytes. The color-coded bands show the error of the measurements.

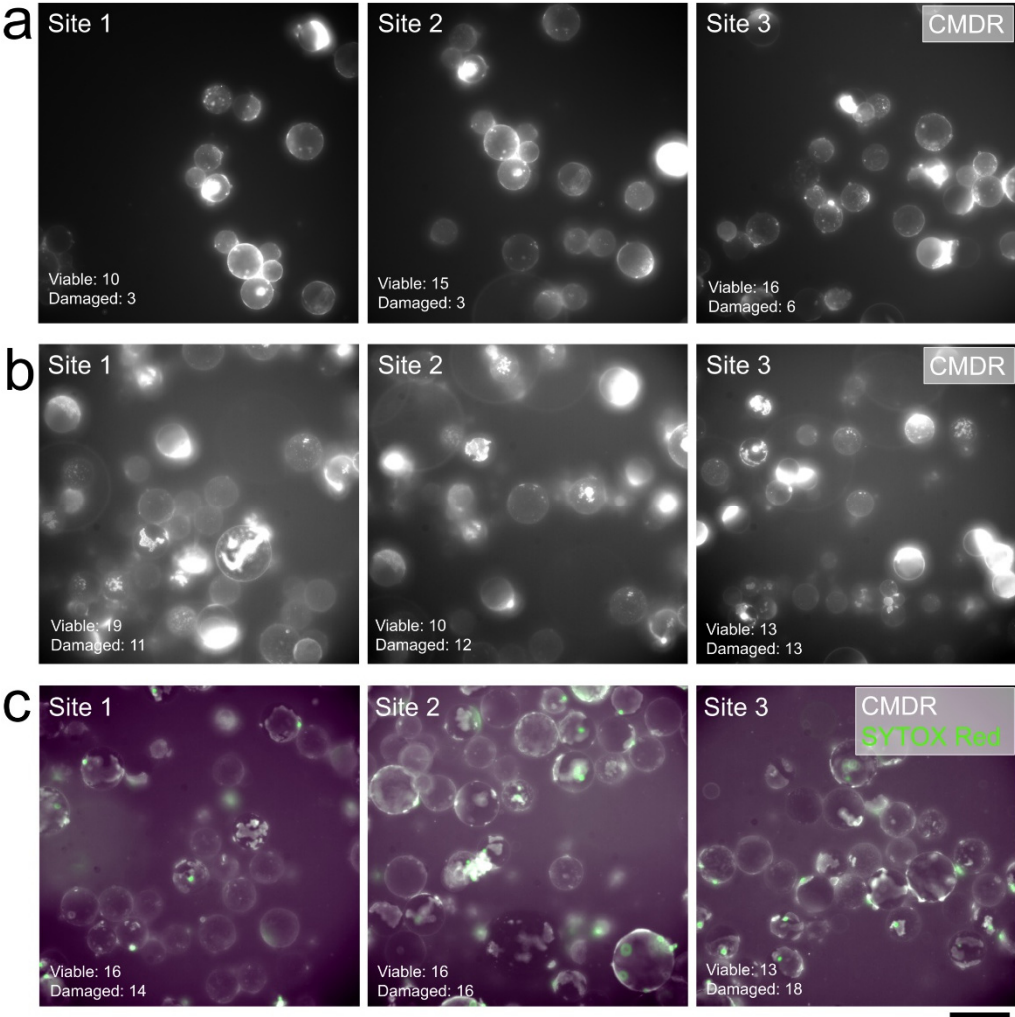


Figure S4. Adipocyte preservation and viability measurements after being isolated from visceral AT presented on different biological replicates (a-c). a) An estimated viability of 70-80% using CellMask Deep Red plasma membrane stain to track membrane rupture and localized accumulation of the stain. b) An estimated viability of 50-70% using the same stain. c) An estimated viability of 40-60% using the combination of CellMask Deep Red (in gray) and SYTOX Red nucleic acid stain (in green), with the distinct features nicely colocalized on the damaged structures. Scale bar is 100 μm .

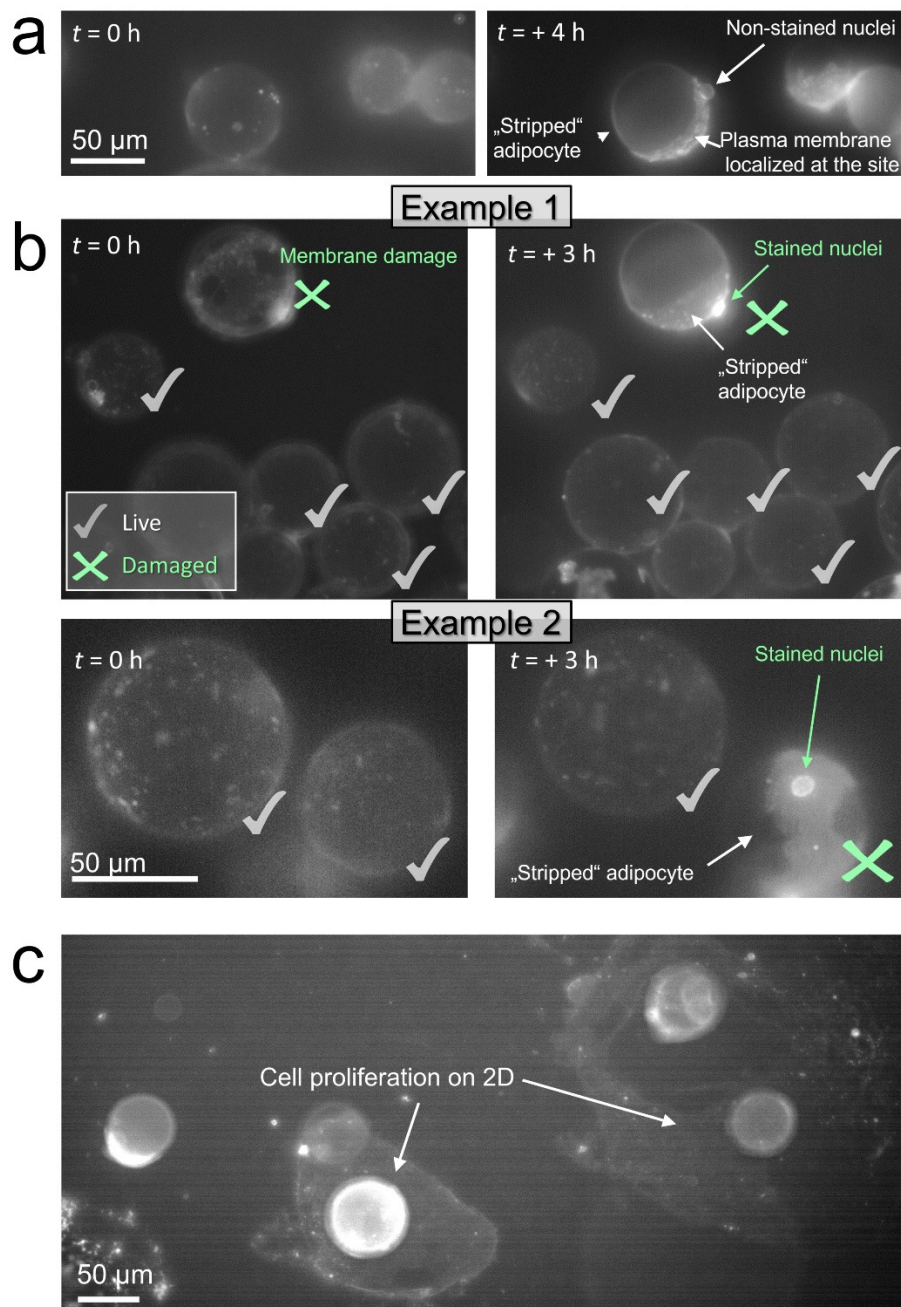


Figure S5. Evaluation of the viability of isolated mature adipocytes for further LD dynamics experiments. (a) Ruptured plasma membrane with possibly retained structural integrity due to non-stained nuclei. (b) The two exemplary cases where the remodeled/ruptured plasma membrane correlates with nuclear labeling, indicating cellular damage/death (marked in green). Adipocytes with a homogeneously stained plasma membranes (checkmarks) remain highly viable, as indicated by the live/dead assay. (c) Cell proliferation on the transwell surface indicates adipocyte dedifferentiation. Imaging was performed using a $20\times$ objective ($NA = 0.45$) with fluorescent labeling of the plasma membrane (CellMask Deep Red, Invitrogen) and nuclei (SYTOX Deep Red).

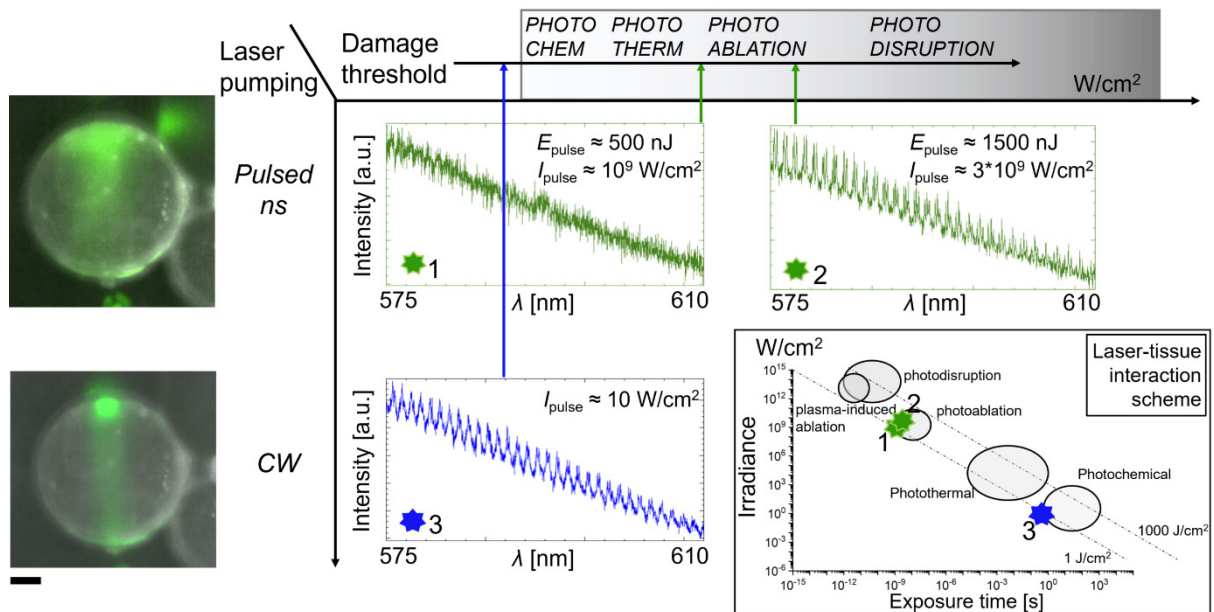


Figure S6. Performance of pulsed and CW pump laser sources for safe WGM-based biosensing applications on mature adipocytes. Due to the non-ideal sphericity and smoothness of LDs in live adipocytes, which are locally disturbed by the cytoskeleton and the imbalance of surrounding mechanical forces, high laser doses/irradiance per pulse (E_{pulse}/I_{pulse}), capable of inducing a photoablation-damaging effect, are commonly required to introduce WGM lasing on adipocytes (2 - green spectra on the right). By introducing an alternative approach using a cost-efficient CW laser, slightly lower performance in spectral resolution and SNR was achieved (3 - blue spectra), but with negligible damaging effects, as shown with the arrow and schematically depicted in the laser-tissue interaction map on the bottom right (adapted from ¹). Scale bar is 10 μ m.

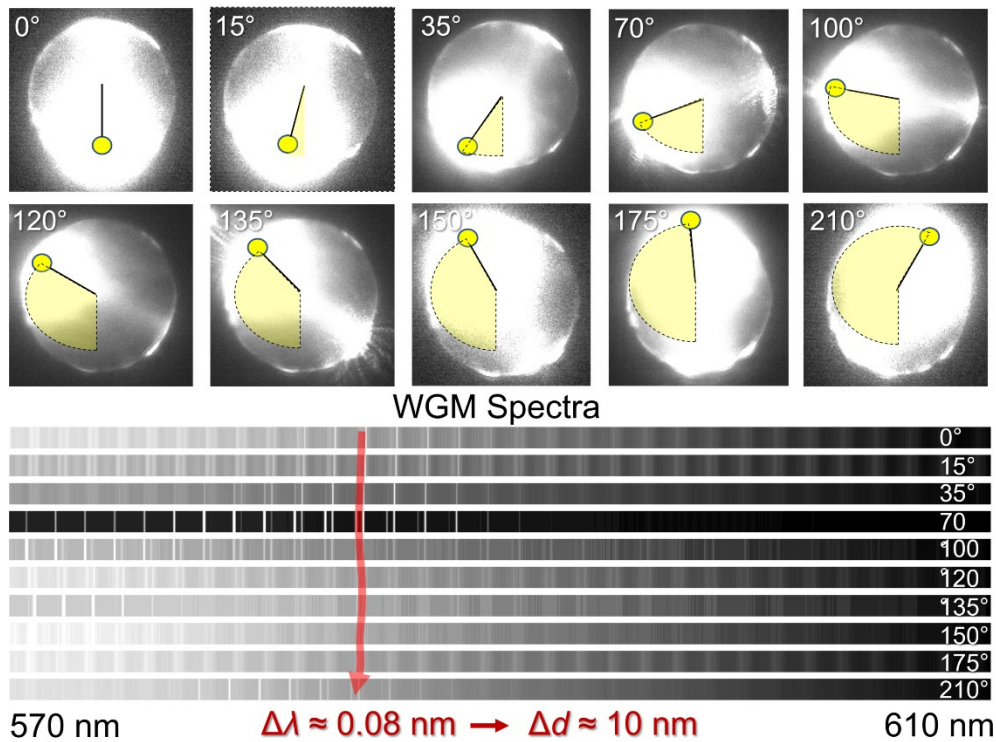


Figure S7. Measurement of the LD sphericity by changing the pump laser position around its circumference. Acquired spectra at different positions, from angle 0° to 210° , reveal deviation from complete sphericity for up to $\Delta\lambda = 0.08$ nm (red arrow), which accounts for the diameter change of up to $\Delta d = 10$ nm, lower than typical changes induced by external stimuli.

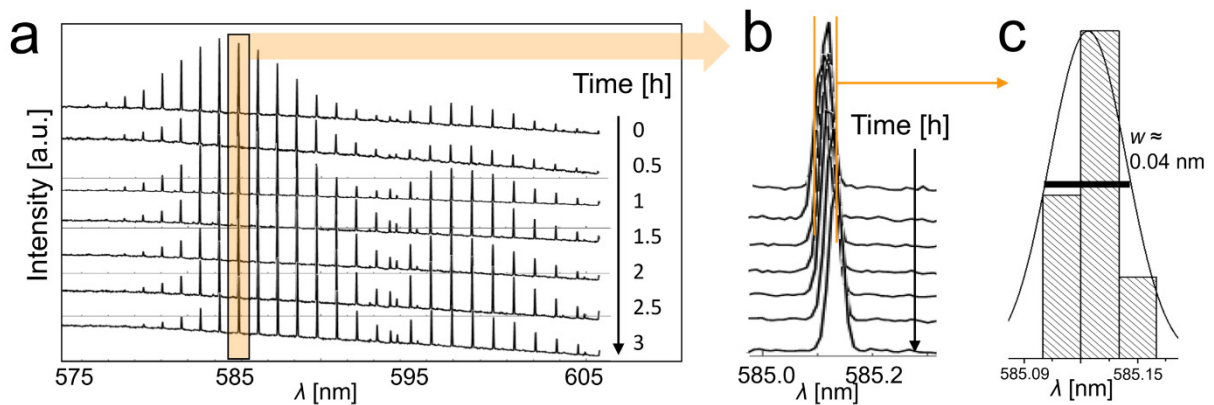


Figure S8. Measurement of the scatter of the acquired multiple spectra on a stable LD throughout our typical time experiment using a pulsed laser. a) WGM spectra performed in a 3-hour time interval with 0.5-hour time steps. b) A slight scatter and a directional trend (red shift) of the spectra as shown on a single eigenmode at $\lambda = 585.13$ nm. c) Distribution of peak positions gathered from multiple spectra.

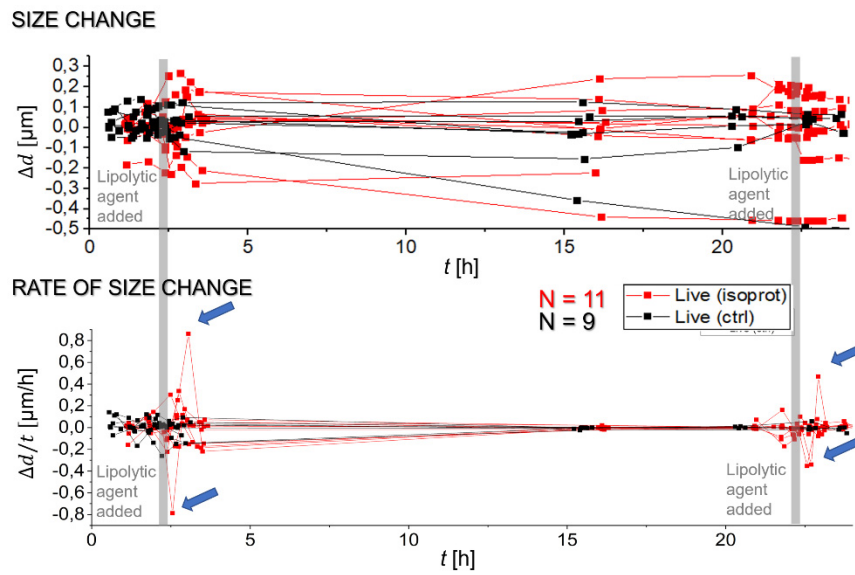


Figure S9. Adipocyte metabolic response via measurements of LD size (Δd) and rate of size change ($\Delta d/t$) to external stimuli induced by isoproterenol (connected data points in red). The data reveal adipocyte heterogeneity and a rapid, transient effect on individual cells (marked with the blue arrow), where the rate of size change oscillates significantly, which is not observed in the control.

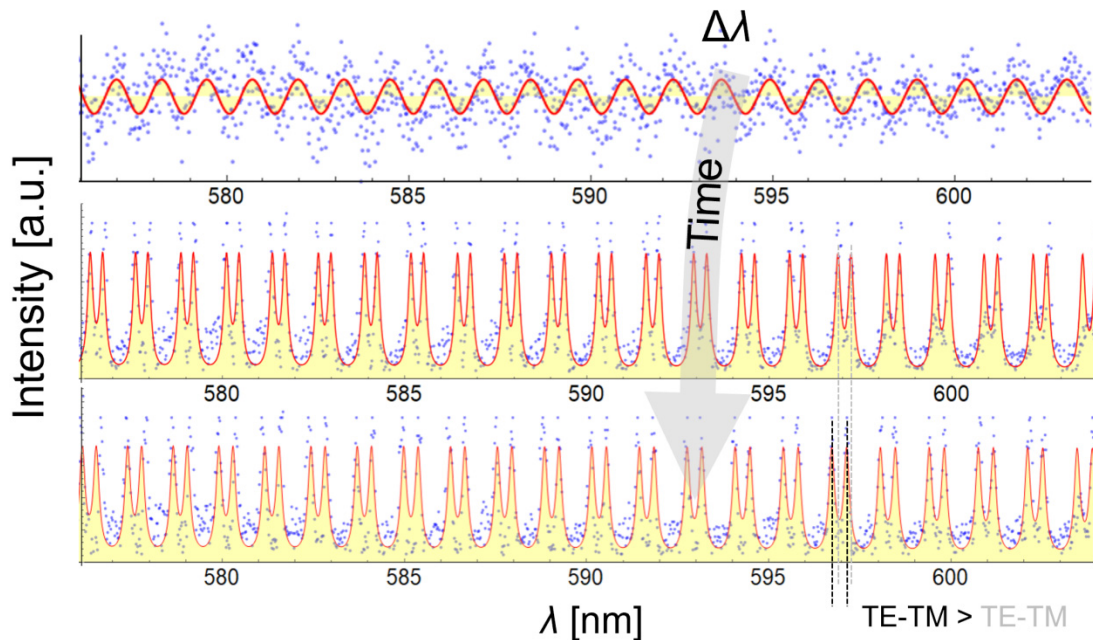


Figure S10. Detailed analysis and fitting of WGM spectra (in red) for the determination of LD size in a dynamically active adipocyte. A significant spectral shape change was observed between the first and second time points, indicating cellular damage or plasma membrane

rupture, which was later confirmed optically (see Figure 5c). A detailed analysis has also revealed a slight but measurable increase in TE and TM mode splitting (black and gray dashed lines), characterized by a decrease in the refractive index in the cellular cytoplasm, indicating dilution induced by plasma membrane rupture.

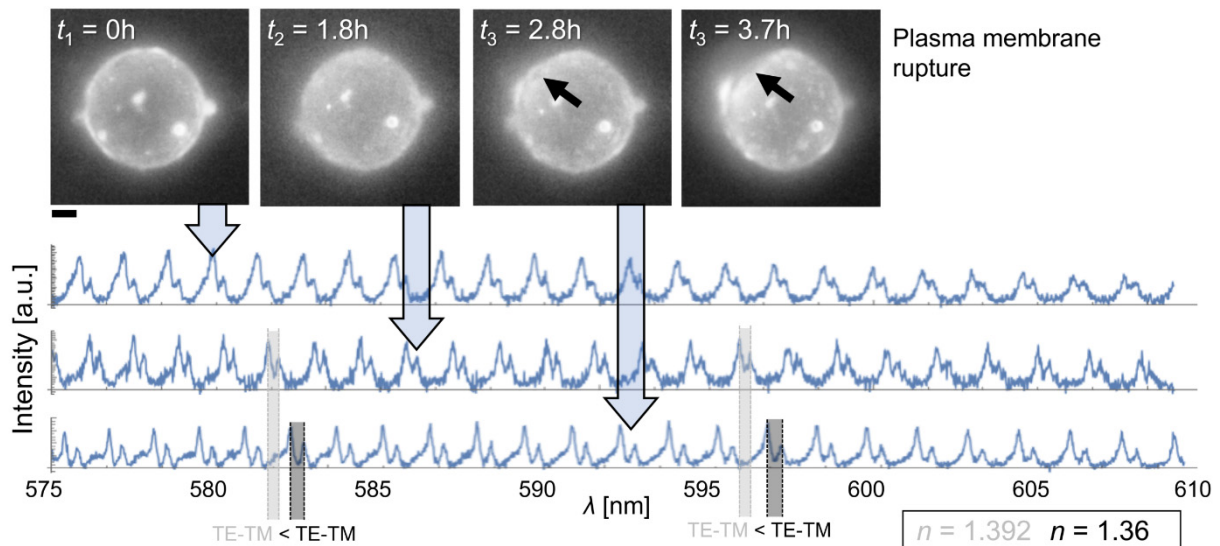


Figure S11. An example of significantly increased TE and TM mode splitting in the WGM spectra is shown between the second and third time points (see the width of the gray bars showing the splitting). This spectral change, characterized by a measurable decrease in the refractive index of the cellular cytoplasm around the LD, is correlated with plasma membrane rupture, as nicely observed in the last time point (see the black arrow). Scale bar is 10 μm .

Supplementary note A

In some cases of cellular disruption, with the membrane appearing localized at one side of the "stripped" adipocyte, the membrane plausibly retained its structural integrity, as observed through non-stained nuclei (Figure S5a), which would otherwise be stained (Figure S5b). This result suggests a potential, albeit unconventional, mechanism for preserving the function of cellular core components during mechanical/physical, or metabolic external stress. The observed behavior was not the case for LDs, which, once partially secreted, had not shown any dynamic activity, indicating arrested metabolic activity and/or cellular damage, as

discussed later. Plasma membrane remodeling may not only result from cellular damage but also participate in the process of adipocyte dedifferentiation ², as observed through cell proliferation on 2D (Figure S5c). Acknowledging all the complexity of the studied biological system, we have focused solely on mature, non-differentiated adipocytes with the preserved structural and functional integrity of both the plasma membrane and LDs. In this context, it was essential to stain both nuclei and the plasma membrane.

Supplementary note B

Individual WGM eigenmodes seem to exhibit a slight directional trend with time (red shift in Figure S7b). Besides instrumentation noise, this trend could be a consequence of physical changes within LD and its direct surroundings related to the possible changes in the temperature (ΔT). The fluctuation of $\Delta T = 1$ °C would introduce the relative change in $\Delta n/n$ within LD and in the surrounding water to a similar extent, ranging between 0.0002 and 0.0001 ^{3,4}, to the minimal relative change in spectra, $\Delta\lambda/\lambda$, that can be observed with the spectrometer with its achievable resolution.

References

- (1) Keiser, G. Light-Tissue Interactions. In *Biophotonics: Concepts to Applications*; Keiser, G., Ed.; Springer Nature: Singapore, **2022**; pp 169–221. DOI: 10.1007/978-981-19-3482-7_6.
- (2) Kim, J.; Park, K.-Y.; Choi, S.; Ko, U. H.; Lim, D.-S.; Suh, J. M.; Shin, J. H. Ceiling Culture Chip Reveals Dynamic Lipid Droplet Transport during Adipocyte Dedifferentiation via Actin Remodeling. *Lab Chip* **2022**, 22 (20), 3920–3932. DOI: 10.1039/D2LC00428C.
- (3) Yanina, I. Y.; Lazareva, E. N.; Tuchin, V. V. Refractive Index of Adipose Tissue and Lipid Droplet Measured in Wide Spectral and Temperature Ranges. *Appl. Opt., AO* **2018**, 57 (17), 4839–4848. DOI: 10.1364/AO.57.004839.
- (4) Schiebener, P.; Straub, J.; Levelt Sengers, J. M. H.; Gallagher, J. S. Refractive Index of Water and Steam as Function of Wavelength, Temperature and Density. *Journal of Physical and Chemical Reference Data* **1990**, 19 (3), 677–717. DOI: 10.1063/1.555859.